# MICRO-OPTO-MECHANICAL STRUCTURES FOR THE INFRARED SPECTRAL RANGE FABRICATED BY TWO-PHOTON POLYMERIZATION

by

Victoria Paige Stinson

A dissertation submitted to the faculty of
The University of North Carolina at Charlotte
in partial fulfillment of the requirements
for the degree of Doctor of Philosophy in
Optical Science and Engineering

Charlotte

2024

Approved by:

Dr. Tino Hofmann

Dr. Glenn D. Boreman

Dr. Menelaos K. Poutous

Dr. Andrew R. Willis

# ABSTRACT

VICTORIA PAIGE STINSON. Micro-Opto-Mechanical Structures for the Infrared Spectral Range Fabricated by Two-Photon Polymerization. (Under the direction of DR. TINO HOFMANN)

Micro-optics have become an essential component in many modern technologies. This can be credited to the perpetually growing needs of communication bandwidths for increased processing power in smaller volumes. With this push to miniaturize systems, micro-optics found its foundation. Initially, micro-optics encompassed micro-scale refractive lenses and simple diffractive optics. Since initial applications in the latter twentieth century, the field of micro-optics has greatly expanded. Micro-optics now encompasses research in areas such as integrated optics, micro-electromechanical systems (MEMS), quantum technology, sensing, energy harvesting, and metamaterials. In its current stage, dynamically tunable micro-optics are crucial to providing additional processing power without increasing volume. Micro-structured optics comprise a subsection of micro-optics where the optical response is manipulated by some sub-wavelength or wavelength-scale structures. The most common example of micro-structured optics are diffractive gratings, but more recently developed configurations such as metamaterials and structures such as photonic crystals also fall within this scope. One challenge in developing micro-structured optics are restrictions in terms of geometric freedom and extensive prototyping times. As a solution to some of these challenges, rapid prototyping techniques such as additive manufacturing have been employed in the development of complex two- and three-dimensional micro-structured optics. Two-photon polymerization, a direct laser writing process, has become a widely accepted approach for the development of micro-structured optics. Two-photon polymerization provides nano-scale feature sizes, resolutions which surpass the diffraction limit of the light source. Many of the resins compatible with this technique are transparent for broad regions in the visible and infrared spectral ranges.

This allows micro-optics to be fabricated without necessitating a secondary processing step. In search of ways to provide additional degrees of tuning in micro-optics, the unique properties of these two-photon compatible resins can be exploited. In this study, dynamically tunable micro-structured optics are developed by two-photon polymerization. Being a polymer, the fabricated structures have unique mechanical properties when compared with conventional glass and metal optics. Utilizing this quality, the structures are designed such that their optical response is sensitive to induced mechanical stress or strain. Both sub-wavelength and wavelength-scale micro-structured arrays were investigated for this mechanical tuning. In each case, changes in the structure's geometry due to mechanical stimuli resulted in a change in the optical response. In combination with a MEMS device, the investigated structures could have applications in integrated optics, mechanical sensing and beamsplitting, and tunable bandgap filtering.

# ACKNOWLEDGEMENTS

This work would not have been possible without the support I received along the way. I would like to first thank my advisor, Dr. Tino Hofmann, for helping me become a more confident and capable individual in my field and for being not only an excellent mentor but also a friend. I would also like to thank my research group Dr. Serang Park, Micheal McLamb, Nuren Shuchi, and Dustin Louisos for their support in this work and their quick aid when challenges inevitably occurred. I am truly grateful for the dynamic we maintained of acting as a team to see projects through from the initial design to writing final manuscript.

I would like to also express gratitude to the faculty of the Department of Physics and Optical Science, especially Dr. Glenn Boreman, Scott Williams, and Dr. Menelaos Poutous, who aided in various aspects of the writing and experimental investigations included in this dissertation. Thank you for always making time to help me to better understand the methods of my research.

I would like to acknowledge the financial support I received which made this research possible from the Graduate Assistant Support Plan (GASP), the National Science Foundation within the Center for Metamaterials, and the Department of Defense Science, Mathematics and Research for Transformation (SMART) Scholarship.

Finally, I would like to thank my family, friends, coaches, and teachers who each played a critical role in my professional and academic growth. I am thankful for my fiancé Michaela who has been by my side at every stage of my higher education. Thank you to my mother for supporting me through this journey, I could not have made it here without you. I see the sacrifices you have made to help my sister and I become our best selves. I especially must thank my older sister Samantha, who tackled many challenges before me and helped me through countless road blocks as we shared the same love for science.

# TABLE OF CONTENTS

# LIST OF FIGURES

# CHAPTER 1: INTRODUCTION

## 1.1 Overview

Over the last century, there has been an ever-prevalent push to miniaturize technology without compromising processing power. When considering this, one commonly thinks of computer systems. When first introduced in the 1940s, these computer systems needed the space of an entire floor to provide sufficient processing power for computation. As advances have been made, powerful and compact computer systems small enough to fit in the palm of your hand have become a normal part of our everyday life. While huge leaps have been made, the need for smaller systems has only increased.

The fields of communication and sensing technology is one of the main drivers of miniaturization. The size of a system is generally limited by the space needed for the processing components. Novel processing elements are needed to go beyond the limits imposed by current technology. In the same way digital electronics were developed to overcome the limitations of analog electronics, micro-optics have been developed to surpass the limits of macroscopic optics [1]. In the early 1990s, micro-optics demonstrated superior function for beam steering and optical fiber coupling [2]. As the applications of micro-optics expands, their ability to be dynamically tunable is crucial [3].

One method of manipulating the optical response of micro-optics is by mechanical means. Micro-optical devices which rely on this mechanical actuation to manipulate light are termed micro-opto-electro-mechanical systems (MOEMS) [2]. A simple example of a MOEMS device would be a micro-mirror array where the individual mirrors can be mechanically controlled. The major applications of MOEMS are in areas such as fiber optics, optical scanning, display, imaging, and adaptive optic technology [4].

Fabrication of micro- and nano-scale optics by additive manufacturing has become widely accepted [5]. This fabrication approach allows more complex geometries to be developed than what is possible by top-down etching and deposition techniques. While there are many additive manufacturing methods appropriate for the fabrication of micro-optics, two-photon polymerization has demonstrated superior capabilities in terms of spatial resolution. Minimum feature sizes on the order of hundreds of nano-meters are attainable using commercially available systems [6]. Many of the photo-sensitive monomers employed with this technique are transparent for regions of the visible and infrared spectral range, allowing for micro-optics to be fabricated in a single processing phase [7, 8].

While there is clear interest in combining optical and mechanical capabilities in a single device, reports on their development by two-photon polymerization are scarce [9]. The majority of research in this space is focused on the development of novel static optics [10] or characterization of the mechanical properties [11, 12]. The work presented in this dissertation aims to combine the optical and mechanical potential of two-photon polymerized structures. Several novel mechanically sensitive micro-optics are developed by two-photon polymerization and their mechanical and optical qualities are characterized.

In the following sections of Chapter 1, the design and fabrication approaches used to develop the mechanically sensitive micro-optics investigated in this work will be discussed. Two optical models are employed in order to accurately render arrays which fall in either the sub-wavelength or wavelength-scale regime. Mechanical modeling is conducted by finite-element method simulation, a well established technique [13]. Centric to this investigation, is the fabrication of these micro-structured optics by two-photon polymerization, a direct laser writing technique. Being that the fabricated structures are polymers, which are largely transparent in the infrared spectral range, their favorable optical and mechanical properties can be exploited.

In Chapter 2, a one-dimensional photonic crystal with a transmissive defect mode is designed and experimentally realized for the first time by two-photon polymerization. The defect resonance's sensitivity to a common fabrication error, layer thickness non-uniformity, is discussed. The use of a scaling factor to compensate for variation in swelling and contraction between layers of varying density is implemented for the first time.

In contrast to the static photonic crystal discussed in Chapter 2, the investigations of Chapter 3 involve mechanically tunable photonic crystals. In these studies, mechanically sensitive constituents are introduced to certain layers of the photonic crystal to allow tuning of the layer thicknesses. By mechanically compressing the photonic crystals, it is experimentally verified that the optical response can be varied. Mechanical tuning of the photonic bandgap (Section 3.1) as well as tuning of a defect resonance (Section 3.2) are demonstrated.

Chapter 4 introduces a design where the micro-structured arrays are no longer in the sub-wavelength regime. In Section 4.1, slanted wire diffraction gratings are investigated for their compatibility with two-photon polymerization and their sensitivity to mechanical tuning is studied numerically. With the promising results of this numerical investigation, preliminary experiments were conducted. A slanted wire grating was designed for visible operation, the results of the experimental study are outlined in Section 4.2.

The key outcomes of these studies as well as the future project directions are discussed in Chapter 5. Structures fabricated by two-photon polymerization have advantages with respect to design freedom and prototype times when compared to alternative techniques. However, there are challenges in terms of serial processing and scalability. These qualities must be considered when selecting an appropriate application space. Potential applications of the novel optical structures developed in this study may range from fundamental uses such as tunable bandgap filtering [14, 15] to more sophisticated applications such as diffractive integrated optics [16, 17].

## 1.2 Modeling Micro-Structured Optics

Several modeling techniques were implemented during this study. A mechanical model is used to determine how the structure will deform as a function some applied stress or strain. Using these conditions, the micro-structure's optical response can be optimized to take advantage of these deformations. The selection of an appropriate optical model depends mainly on the minimum size of the features within the array compared to the operation wavelength.

For arrays which have sub-wavelength features, an effective medium approximation can be used to describe the array's dielectric properties. The Bruggeman effective medium approximation which is implemented here is calculated by [18]:

$$\begin{aligned}\varepsilon_{\mathrm{low}}^{\mathrm{eff}}(\omega, f_{\mathrm{i}}) \quad = \quad & \frac{1}{4}\Big\{(3f_{\mathrm{i}}-1)\varepsilon_{\mathrm{i}}(\omega)+(2-3f_{\mathrm{i}})\varepsilon_{\mathrm{h}}(\omega)\pm \\ & \Big([(3f_{\mathrm{i}}-1)\varepsilon_{\mathrm{i}}(\omega)+(2-3f_{\mathrm{i}})\varepsilon_{\mathrm{h}}(\omega)]^2+\varepsilon_{\mathrm{i}}(\omega)\varepsilon_{\mathrm{h}}(\omega)\Big)^{\frac{1}{2}}\Big\}.\end{aligned} \tag{1.1}$$

The dielectric properties of the inclusions and the host medium are given by $\varepsilon_{\mathrm{i}}$ and $\varepsilon_{\mathrm{h}}$, respectively. In these investigations the host medium is air, i.e., $\varepsilon_{\mathrm{h}} = 1$, while the inclusions are the array material. The array material is a photosensitive resin compatible with fabrication by two-photon polymerization $\varepsilon_{\mathrm{i}}(\omega) = \varepsilon^{\mathrm{resin}}(\omega)$. The volume ratio between the inclusions and the host medium is described by the volumetric fill factor $f_i$.

Using the effective medium approximation, the dielectric properties within a given array can be adjusted by increasing or decreasing the density of resin to air. Using this principle, the dielectric properties within a structure can be tuned by altering the array density. For structures where this density-dependent dielectric control is varied along the optical axis, a stratified-layer optical model can be applied [19]. The dielectric properties are assumed to be constant within a given layer and interfaces are assumed to be plane parallel. The cumulative effects of variations in layer thickness and density can then be tuned to produce a desired spectral response.

As the feature size nears the operation wavelength, diffraction effects must be considered. For modeling periodic micro-structured optics in this regime, a rigorous coupled wave analysis (RCWA), also known as the Fourier modal method, can be implemented. As the latter name implies, computations are taken in Fourier-space. RCWA has been used to model the optical response of diffraction gratings for several decades. Detailed assessments of the use of RCWA in modeling diffraction gratings can be found in Refs. 20 and 21.

While RCWA provides details on the population of diffraction orders, a separate computation is needed to determine the angle at which orders will propagate. For one-dimensional gratings, the grating equation can be applied:

$$\begin{aligned} n_{\mathrm{t}} \sin\theta_{\mathrm{t}m} - n_{\mathrm{i}} \sin\theta_{\mathrm{i}} &= m\left(\tfrac{\lambda}{\Lambda}\right)\sin\phi, \\ m &= 0, \pm1, \pm2, \pm3\ldots \end{aligned} \tag{1.2}$$

by knowing the refractive indices of the incident ($n_{\mathrm{i}}$) and transmitted ($n_{\mathrm{t}}$) mediums, the operation wavelength ($\lambda$), the grating period ($\Lambda$), and the angle of incidence ($\theta_{\mathrm{i}}$), the angle of the transmitted $m$-th order can be determined ($\theta_{\mathrm{t}m}$).

In order to design micro-structured optics which are sensitive to mechanical stimuli, a finite-element method is used to predict the structure's deformation. A commercially available finite-element software (COMSOL Multiphysics®, Burlington, MA, USA) was employed for mechanical simulations. Within the Structural Mechanics module, the overall deformation of a structure due to applied stress or strain can be simulated if the mechanical properties are known.

To describe how the overall structure may deform, the structure is represented as a mesh grid composed of smaller parts, termed *finite-elements*. As the materials used to fabricate these structures are polymers under small perturbations of stress or strain, the material can be treated as an isotropic linear elastic material [22]. Under these conditions, the following 6 × 6 elasticity matrix is solved for each finite-element defined by the mesh grid [23]:

$$D = \frac{E}{(1+v)(1-2v)} \begin{bmatrix} 1-v & v & v & 0 & 0 & 0 \\ v & 1-v & v & 0 & 0 & 0 \\ v & v & 1-v & 0 & 0 & 0 \\ 0 & 0 & 0 & \frac{1-2v}{2} & 0 & 0 \\ 0 & 0 & 0 & 0 & \frac{1-2v}{2} & 0 \\ 0 & 0 & 0 & 0 & 0 & \frac{1-2v}{2} \end{bmatrix}, \quad (1.3)$$

where $E$ is Young's modulus and $v$ is Poisson's ratio. The derivation of this matrix from the elastic strain tensor for linear elastic materials is described in detail in Ref. 23.

## 1.3 Fabrication by Two-Photon Polymerization

A designed micro-structured array is synthesized by two-photon polymerization, a direct laser writing technique. In this technique, structures are written by focusing a beam within a photosensitive resin. A schematic of the writing process can be seen in Fig. 1.1. The objective is immersed in a photosensitive resin, shown in the inset. The interface of the substrate is then detected through interference. The beam writes within the resin by the rotation of two fast-scanning galvo mirrors in combination with movement of a three-dimensional piezoelectric motor stage which is connected to the sample holder.

The ellipsoidal volume around the focus where there is enough energy for polymerization to occur is termed the voxel. The voxel dimensions determine the resolution of the fabricated structures. The voxel size is a function of the selected objective magnification and resin as well as the fabrication parameters such as hatching and slicing distances, scan speed, and laser power [24].

A commercially available two-photon polymerization system (Photonic Professional GT, Nanoscribe GmbH, Eggenstein-Leopoldshafen, Germany) is used in this study. The index contrast needed for auto-focusing to the interface between the resin and substrate ($\Delta n$) will vary between 0.03 and 0.10 depending on the selected objective [25]. To fabricate sub-wavelength-scale features for infrared operation, nano-scale resolution is needed. The 63x objective is selected as this magnification provides in plane resolution of 200 nm. For this objective, the necessary index mismatch between

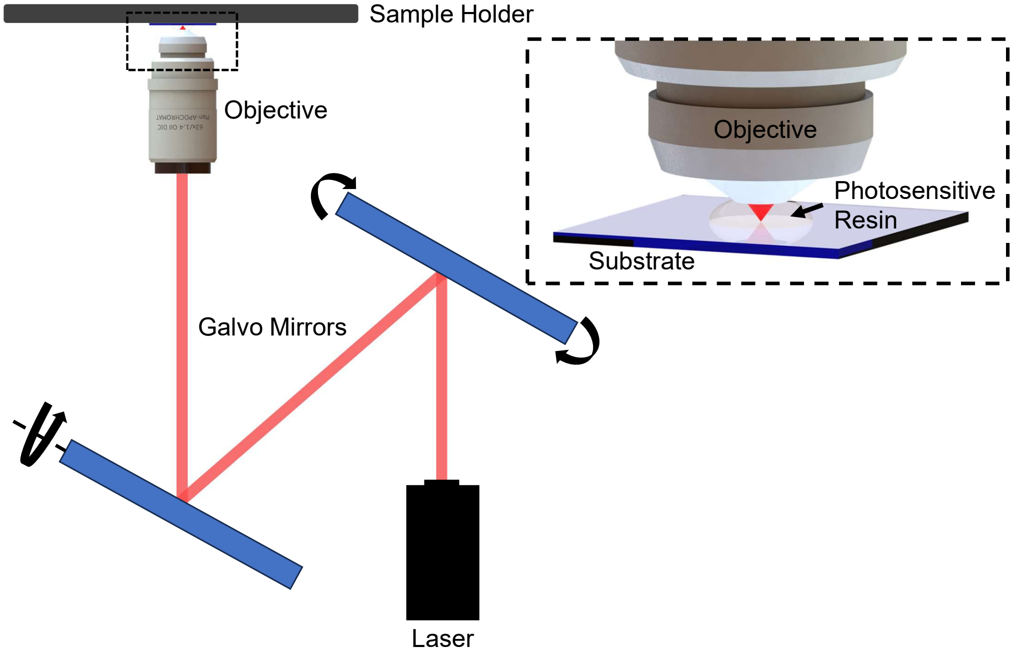

Figure 1.1: Schematic of the two-photon polymerization writing process. The objective is immersed in a compatible photosensitive resin which can be seen in the inset. The structures are then written on the substrate by galvo scanning in combination with movement of a three-dimensional piezoelectric motor stage which controls the sample holder position.

the resin and substrate is $\Delta n > 0.05$. While different resin-substrate combinations can be used to achieve this contrast, it is recommended that the IP-Dip resin and fused silica substrate be used for the highest quality fabrication [25].

It is necessary to select appropriate print parameters based on the designed geometry. Minimum feature size, array size, and internal structure must be considered when selecting these parameters. Higher objective magnification can reduce the voxel size, improving resolution, but requires longer fabrication times. For a given objective, parameters such as laser power, scan speed, and hatching and slicing distances will also affect the voxel size [26]. Hatching and slicing distances are used to set the proximity of adjacent scans in the $x/y$ and $z$ axes, respectively. Selecting an appropriate combination of settings by sequential attempts can be time consuming, in this work, dose matrices are used to more efficiently test various setting combinations. A "test structure" is created which includes a portion of the geometry of the full design, usually the portion which has the smallest feature size. This "test structure" is then fabricated by different combinations of scan speed, laser power, and slicing and hatching distances. The quality of the "test structure" can then be compared between these different combinations, allowing for a setting which provides good structural quality with efficient print times to be selected.

# REFERENCES

[1] B. C. Kress and P. Meyrueis, *Applied digital optics: from micro-optics to nanophotonics*, Hoboken, NJ, John Wiley & Sons, (2009).

[2] P. Joshi, "Advances in Development of MOEMS Devices: A Review," *HELIX* **9**, 5868 (2019).

[3] C. Friese, A. Werber, F. Krogmann, W. Mönch, and H. Zappe, "Materials, effects and components for tunable micro-optics," *IEEJ T. Electr. Electr.* **2**, 232 (2007).

[4] M. E. Motamedi, *MOEMS: Micro-opto-electro-mechanical Systems*, Bellingham, WA, SPIE press, (2005).

[5] A. Zolfaghari, T. Chen, and A. Y. Yi, "Additive manufacturing of precision optics at micro and nanoscale," *Int. J. Extreme Manuf.* **1**, 012005 (2019).

[6] S. O'Halloran, A. Pandit, A. Heise, and A. Kellett, "Two-photon polymerization: fundamentals, materials, and chemical modification strategies," *Adv. Sci.* **10**, 2204072 (2023).

[7] D. B. Fullager, G. D. Boreman, and T. Hofmann, "Infrared dielectric response of nanoscribe IP-dip and IP-L monomers after polymerization from 250 $\text{cm}^{-1}$ to 6000 $\text{cm}^{-1}$," *Opt. Mater. Express* **7**, 888 (2017).

[8] Y. Li, S. Park, M. McLamb, M. Lata, S. Schöche, D. Childers, I. D. Aggarwal, M. K. Poutous, G. Boreman, and T. Hofmann, "UV to NIR optical properties of IP-Dip, IP-L, and IP-S after two-photon polymerization determined by spectroscopic ellipsometry," *Opt. Mater. Express.* **9**, 4318 (2019).

[9] C. Reinhardt, A. Ovsianikov, S. Passinger, and B. N. Chichkov, "Fabrication

of micromechanical and microoptical systems by two-photon polymerization," *P. Soc. Photo.-Opt. Ins.* **6466**, 194 (2007).

[10] H. Wang, W. Zhang, D. Ladika, H. Yu, D. Gailevičius, H. Wang, *et al.*, "Two-Photon Polymerization Lithography for Optics and Photonics: Fundamentals, Materials, Technologies, and Applications," *Adv. Funct. Mater.* **33**, 2214211 (2023).

[11] M. Carlotti and V. Mattoli, "Functional materials for two-photon polymerization in microfabrication," *Small* **15**, 1902687 (2019).

[12] A. K. Nguyen and R. J. Narayan, "Two-photon polymerization for biological applications," *Mater. Today* **20**, 314 (2017).

[13] O. C. Zienkiewicz and R. L. Taylor, *The finite element method: solid mechanics*, vol. 2, Oxford, Butterworth-Heinemann, (2000).

[14] H. Jiang, H. Chen, H. Li, Y. Zhang, and S. Zhu, "Omnidirectional gap and defect mode of one-dimensional photonic crystals containing negative-index materials," *Appl. Phys. Lett.* **83**, 5386 (2003).

[15] S. Li, G. Feng, Y. Liu, M. Wu, X. Zhao, F. Sun, *et al.*, "Omnidirectional near-infrared narrowband filters based on defective mirror-symmetry one-dimensional photonic crystals containing hyperbolic metamaterials," *Opt. Laser Eng.* **176**, 108107 (2024).

[16] T. Fu, Y. Zang, Y. Huang, Z. Du, H. Huang, C. Hu, *et al.*, "Photonic machine learning with on-chip diffractive optics," *Nat. Commun.* **14**, 70 (2023).

[17] X. Pan, H. Zuo, H. Bai, Z. Wu, and X. Cui, "Real-time wavefront correction using diffractive optical networks," *Opt. Express* **31**, 1067 (2023).

[18] W. Cai and V. M. Shalaev, *Optical metamaterials*, vol. 10, Springer, (2010).

[19] Y. Li, D. Fullager, S. Park, D. Childers, R. Fesperman, G. Boreman, and T. Hofmann, “High-contrast infrared polymer photonic crystals fabricated by direct laser writing,” *Opt. Lett.* **43**, 4711 (2018).

[20] M. Moharam and T. Gaylord, “Rigorous coupled-wave analysis of planar-grating diffraction,” *JOSA* **71**, 811 (1981).

[21] T. K. Gaylord and M. Moharam, “Analysis and applications of optical diffraction by gratings,” *Proceedings of the IEEE* **73**, 894 (1985).

[22] J. S. Bergstrom, *Mechanics of solid polymers: theory and computational modeling*, Norwich, NY, William Andrew, (2015).

[23] *Structural Mechanics Module User’s Guide*, COMSOL Multiphysics, Burlington, MA, 198–243, (2023).

[24] Y.-L. Zhang, Q.-D. Chen, H. Xia, and H.-B. Sun, “Designable 3D nanofabrication by femtosecond laser direct writing,” *Nano Today* **5**, 435 (2010).

[25] *Photonic Professional (GT) User Manual*, Nanoscribe GmbH, Eggenstein-Leopoldshafen, Germany, (2017).

[26] D. Tan, Y. Li, F. Qi, H. Yang, Q. Gong, X. Dong, and X. Duan, “Reduction in feature size of two-photon polymerization using SCR500,” *Appl. Phys. Lett.*, **90**, 071106, (2007).

# CHAPTER 2: PHOTONIC CRYSTALS FABRICATED BY TWO-PHOTON POLYMERIZATION

One-dimensional photonic crystals composed of alternating layers with high- and low-density were fabricated using two-photon polymerization from a single photosensitive polymer for the infrared spectral range.[1] By introducing single high-density layers to break the periodicity of the photonic crystals, a narrow-band defect mode is induced. The defect mode is located in the center of the photonic bandgap of the one-dimensional photonic crystal. The fabricated photonic crystals were investigated using infrared reflection measurements. Stratified-layer optical models were employed in the design and characterization of the spectral response of the photonic crystals. A very good agreement was found between model-calculated and measured reflection spectra. The geometric parameters of the photonic crystals obtained as a results of the optical model analysis were found to be in good agreement with the nominal dimensions of the photonic crystal constituents. This is supported by complimentary scanning electron microscope imaging which verifies the model-calculated, nominal layer thicknesses. Conventionally, accurate fabrication of such structures would require layer-independent print parameters, which are difficult to obtain with high precision. In this study an alternative approach is employed using density-dependent scaling factors, introduced here for the first time. Using these scaling factors a fast and true-to-design fabrication of layers with significantly different surface-to-volume ratios is enabled. The reported observations furthermore demonstrate that the location and amplitude of defect modes is extremely sensitive to any layer thickness

---

[1] Reprinted with permission from V. P. Stinson, S. Park, M. McLamb, G. D. Boreman, and T. Hofmann, "Photonic Crystals with a Defect Fabricated by Two-Photon Polymerization for the Infrared Spectral Range," *Optics* **2**, 284 (2021). © 2021, MDPI.

non-uniformities in the photonic crystal structure. Considering these capabilities, one-dimensional photonic crystals engineered with defect modes can be employed as narrow band filters for instance, while also providing a method to quantify important fabrication parameters.

## 2.1 Introduction

Photonic crystals are capable of providing nearly perfect reflection in a narrow spectral window, referred to as the photonic bandgap, which can be easily tuned for a desired spectral range by tailoring the constituents of the photonic crystal [1–15]. Early motivation for the development of photonic crystals was centered around their unique applications in quantum electronics and quantum optics [16]. Photonic crystals can be categorized as one-, two-, and three-dimensional, depending on the spatial arrangement of constituents of the photonic crystals which will determine their application [17]. One-dimensional photonic crystals are the simplest of these geometries and can be realized by the periodic arrangement of transparent layers with different dielectric properties [1, 2, 4–7, 11–14, 17].

It has been demonstrated that defects in the spatially periodic arrangement of the dielectric layers induce defect states in the photonic bandgap, which can result in narrow transmission bands within a band of high reflectivity [4–7, 13, 14, 17]. For one-dimensional photonic crystals a defect mode can be introduced by the addition of a layer which disrupts the dielectric periodic arrangement of the surrounding layers. Such photonic crystals have been designed for several applications including enhanced Faraday rotators [4], omnidirectional bandgap filters [5], sensors [18, 19], and narrow band filters [20].

Several techniques have been demonstrated for the fabrication of one-dimensional photonic crystals. The most commonly used method is spin coating, which allows the fabrication of sequences of thin films with different dielectric properties [10, 21]. Other methods include self-assembly, which uses a layer-by-layer approach, top-down etching, chemical vapor deposition, physical vapor deposition, and molecular beam epitaxy [10, 22]. Direct laser writing using two-photon polymerization has been recently used to fabricate photonic crystals [9, 11, 23]. One of the main advantages of two-photon polymerization is its capability to synthesize virtually arbitrary geometries with critical dimensions on the order of a few hundred nanometers. This enables the fabrication of photonic crystals from a single dielectric material by alternating layers of high- and low-density [11]. The scale of photonic crystals fabricated by two-photon polymerization is often limited due to the serial nature of the two-photon polymerization process which can lead to extensive fabrication times. Novel approaches have aimed for the acceleration of the fabrication process by combining traditional interference lithography and two-photon lithography [24]. Using this approach three-dimensional photonic crystals with controlled defects have very recently been demonstrated.

The accuracy by which structures can be fabricated using the two-photon polymerization approach is greatly affected by the choice of focusing objective and the fabrication parameters used, such as laser power, scan speed [25–27], and laser-beam paths governed by slicing and hatching distances [28]. Any of these parameters will affect the volume over which polymerization occurs. The voxel size of the instrument depends on a wide range of parameters and therefore can alter the fabricated sample geometry. While the power density is determined by the scan speed and the nominal laser power, the slicing and hatching distance will affect the resolution and integrity of features in the horizontal plane and vertical plane, respectively [28]. Determining the optimal settings for these parameters is indispensable to achieve a desired spectral response.

The position of the photonic bandgap in a one-dimensional photonic crystal is sensitive to even small changes in the thickness (±5 nm) as well as changes in the dielectric properties of its constituent layers [11]. Thus it is critical to determine fabrication parameters which result in a true-to-design geometry with minimal variation in layer thickness and dielectric properties across the constituent layers.

In this paper we demonstrate the successful fabrication of one-dimensional photonic crystals with defects that induce narrow transmission bands centered within the photonic bandgap using two-photon polymerization from a single monomer. Experimental data and stratified-layer optical model calculations reveal that that the induced defect modes are extremely sensitive to the layer thickness uniformity of the photonic crystal. In addition, a simple approach for the optimization of two-photon polymerization fabrication parameters for photonic crystals is introduced. Our proposed approach introduces a geometric scaling factor which helps to obtain true-to-design fabrication of photonic crystals while substantially reducing the time required to determine optimal fabrication parameters.

## 2.2 Design, Fabrication, and Characterization

One-dimensional photonic crystals composed of alternating layers of high- and low-density (see Fig. 2.1) were designed using stratified-layer optical model calculations (WVASE32, J.A. Woollam, Co.). Alternating dielectric layers were produced using a two-photon polymerization compatible polymer IP-Dip. The dielectric properties of the compact layers $\varepsilon^{\mathrm{IP-Dip}}(\omega)$ are described by the parameterized model-dielectric-function of polymerized IP-Dip. The model-dielectric-function of this material has been previously established using spectroscopic ellipsometry in the infrared spectral range and is described using a simple mixed oscillator model [29].

The low-density layers consist of sub-wavelength cylindrical pillars which are arranged in a square lattice pattern and are oriented normal to the low-density/high-density interface. The dielectric function of the low-density layers $\varepsilon^{\mathrm{eff}}_{\mathrm{low}}(\omega, f_{\mathrm{i}})$ can be described using the Bruggeman effective medium approximation given by [30]:

$$\begin{aligned}\varepsilon^{\mathrm{eff}}_{\mathrm{low}}(\omega, f_{\mathrm{i}}) &= \frac{1}{4}\Big\{(3f_{\mathrm{i}}-1)\varepsilon_{\mathrm{i}}(\omega)+(2-3f_{\mathrm{i}})\varepsilon_{\mathrm{h}}(\omega)\pm \\ &\Big([(3f_{\mathrm{i}}-1)\varepsilon_{\mathrm{i}}(\omega)+(2-3f_{\mathrm{i}})\varepsilon_{\mathrm{h}}(\omega)]^2+\varepsilon_{\mathrm{i}}(\omega)\varepsilon_{\mathrm{h}}(\omega)\Big)^{\frac{1}{2}}\Big\}.\end{aligned} \tag{2.1}$$

The dielectric properties of the inclusions and the host medium are then given by $\varepsilon_{\mathrm{i}}$ and $\varepsilon_{\mathrm{h}}$, respectively. In our design the host medium is air, i.e., $\varepsilon_{\mathrm{h}} = 1$, while the inclusions consist of polymerized IP-Dip $\varepsilon_{\mathrm{i}}(\omega) = \varepsilon^{\mathrm{IP-Dip}}(\omega)$. The volume ratio between the cylindrical inclusions and the host medium is described by the volumetric fill factor $f_i$.

The effect of a high-density defect layer is explored by comparing the infrared optical response of two photonic crystals. Using simple stratified-layer optical model calculations, the photonic bandgaps of the photonic crystals are designed to be centered at $\omega = 2556$ cm$^{-1}$ ($\lambda = 3.91$ µm). The selection of the wavelength for the photonic bandgaps is based on the dielectric function of IP-Dip which offers a transparent window in the range from 2000 to 3000 cm$^{-1}$ [29]. One crystal is composed of 6 alternating high- and low-density layers. The thicknesses of the high- and low-density layers are designed to be 3.3 µm and 2.8 µm respectively as shown in Fig. 2.1. The volumetric fill factor $f_i$ of the low-density layers is $f_i = 0.2$. The second crystal is identical to the first crystal except for the introduction of a high-density defect layer in the center of the layer stack. The high-density defect layer has a thickness of 5.3 µm and consists of compact polymerized IP-Dip. The base of both photonic crystals is designed to be 49.2 µm x 49.2 µm.

A commercial two-photon polymerization system (Photonic Professional GT, Nanoscribe, GmbH) was used to polymerize a single monomer (IP-Dip) in order to fabricate the one-dimensional photonic crystal structures on a fused silica substrate. It is very well known that the voxel size depends on a number of parameters such as the

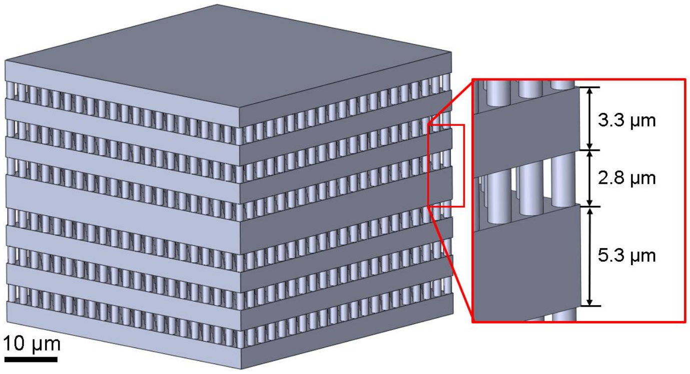

Figure 2.1: CAD model showing the dimensions of the one-dimensional photonic crystal design investigated here. The photonic crystal consists of alternating high-density, compact, layers and low-density layers. The nominal thickness of the high-density layers is 3.3 μm. The low-density layers with a nominal thickness of 2.8 μm are composed of cylindrical pillars with a diameter of 1.2 μm which are arranged in a square-lattice pattern on the surface with a lattice constant of 2.4 μm. The corresponding nominal volumetric fill factor $f_i$ of the low-density layer is $f_i = 0.2$. For the photonic crystal with the high-density defect, the defect layer has a nominal thickness of 5.3 μm and is centered in the layer stack.

objective, choice of monomer, laser power, scan speed, and hatching and slicing distances, for instance [25–28]. Thus the identification of parameters which permit the true-to-design fabrication of complex structures can be difficult and time consuming.

For the photonic crystals discussed here, the volume-to-surface ratios between the low-density and high-density layers differ substantially. As a result, low- and high-density layers are affected differently by the solvent-diffusion-based swelling/contraction which occurs during the rinsing/drying process after the polymerization. This fabrication problem is resolved here by introducing a one-dimensional geometric scaling factor $\gamma_{\text{SF}}$, which provides a layer thickness scaling that is different for high- and low-density layers. The scaling factors were determined using photonic crystals without defects, but otherwise identical designs. For the high-density layers $\gamma_{\text{SF}}$=0.92 and for the low-density layers $\gamma_{\text{SF}}$=1.30 was used.

Following the fabrication, the structures are rinsed in propylene glycol monomethyl ether acetate for 10 minutes, 99.99% isopropyl alcohol for 10 minutes, and then left to air dry for at least 30 minutes. A 63x objective with laser power at 20 mW and scan speed at 500 mm/s was used. Both slicing distance and hatching distance were set to 0.2 µm.

Infrared reflection measurements were carried out for all photonic crystals in the spectral range from 2000 cm$^{-1}$ to 3000 cm$^{-1}$ with resolution 2 cm$^{-1}$ using an IR microscope (HYPERION 3000 Bruker, Inc.) in combination with a FTIR spectrometer (VERTEX 70, Bruker, Inc.). The IR microscope with an annular collection aperture was equipped with a Mercury-Cadmium-Telluride detector. A 15x Cassegrain objective with confocal illumination was used with an aperture setting of 20 µm, resulting in an angular spread of 0.6° with an average angle of incidence of 8.7°. All reflection measurements were normalized to a bulk gold sample using the same aperture settings as employed during the sample data acquisition. A silicon carbide globar was used as a light source. All measurements were performed at room temperature. Stratified-layer optical model calculations obtained using WVASE32 (J.A. Woollam Co.) were employed to analyze the reflection measurements. SEM images, shown in Fig. 2.2 independently demonstrate the quality of the fabrication and the resulting true-to-design dimensions of the fabricated photonic crystal.

## 2.3 Results and Discussion

The experimental reflection data (dashed lines) and best-model calculated reflection data (solid lines) for both crystals are depicted in Fig. 2.3. The major spectral feature is the photonic bandgap which is centered at 2500 cm$^{-1}$ for both photonic crystals. For the photonic crystals with the solid layer defect, a defect mode is formed in the center of the photonic bandgap. The reflection amplitude of the photonic crystal without a defect is 77%, with a high-density defect layer this amplitude is reduced to 62%. The defect mode of the photonic crystal with a high-density defect layer is centered at 2520 cm$^{-1}$ and has a reflection amplitude of 26% with respect to the average bandgap maxima of 62%. A very good agreement was found between the best-fit stratified-layer optical model calculations (solid lines) and the experimental

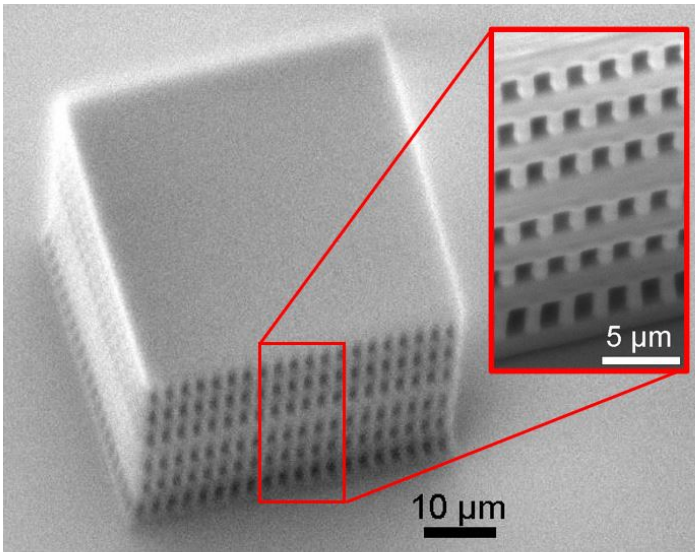

Figure 2.2: Scanning electron microscope (SEM) image taken at an operating voltage of 1kV of the photonic crystal with a defect layer, as described by Fig. 2.1. Inset SEM image taken with an operating voltage of 7 kV.

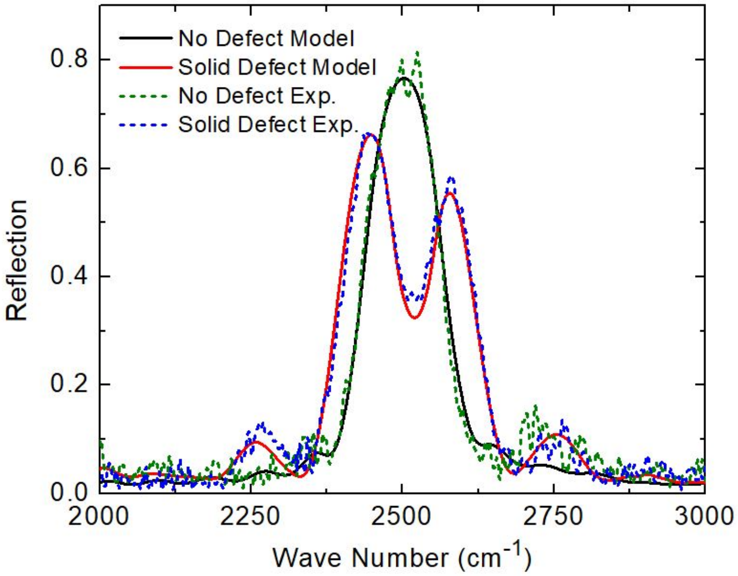

Figure 2.3: Comparison between best-model calculated (solid lines) and experimental (dashed lines) reflection data obtained from identical photonic crystals with and without a solid defect. The spectra are dominated by the photonic bandgap centered at approximately 2500 cm$^{-1}$. The photonic crystal with a solid defect exhibits a defect mode in the middle of the photonic bandgap. Experimental and best-model calculated data are in very good agreement.

reflection measurements (dashed lines) for both photonic crystals.

The optical model is composed of 14 layers: a fused silica substrate, 6 A-B layer pairs of low- and high-density layers and a high-density defect layer in the center following the design shown in Fig. 2.1. The dielectric functions of the glass substrate and IP-Dip used here were previously determined using spectroscopic ellipsometry and were not varied in the model [29, 31]. Eq. (2.1) is used to determine the dielectric function of the low-density layers. During the data analysis, geometrical model parameters were varied simultaneously, including: layer thickness of the low- and high-density layers, layer thickness non-uniformity, and volumetric fill fraction $f_i$. All parameters were adjusted using a Levenberg-Marquardt-based algorithm until the best-match between the model-calculated and experimental reflection data set was obtained. Note that the experimental data sets of both photonic crystals were analyzed simultaneously in order to reduce parameter correlation. The best-model thickness of the low-density layers was determined to be (2.771 ± 0.014) µm, the high-density to be (3.311 ± 0.010) µm, and the high-density defect layer to be (5.240 ± 0.015) µm. The best-model volumetric fill factor was found to be $f_i = 0.296 \pm 0.007$. In order to model the experimental reflection data accurately, layer thickness non-uniformities were taken into account and found to be an average of (2.8 ± 0.1)% for all layers.

The effect of this non-uniformity on the defect mode is illustrated in Fig. 2.4 where stratified-layer optical model calculations for two photonic crystals with a defect are compared. The spectrum plotted with a black dashed line depicts the model-calculated reflection obtained assuming ideal interfaces and the red solid line assumes a 2.8% layer thickness non-uniformity. A photonic bandgap with a centered defect mode can be seen for both models; however, the amplitude of both the photonic bandgap and the defect mode is diminished for the photonic crystal with non-ideal interfaces. The reflection amplitude of the defect mode with perfect layer uniformity is 56% while the amplitude with a 2.8% layer thickness non-uniformity is 26%. Additionally, the average photonic bandgap magnitude is reduced by approximately 5.6% with this non-uniformity present. Our experimental findings corroborate theoretical calculations conducted by T.S. Perova et al. [8] which have shown that layer thickness non-uniformities induce a reduction in the bandgap amplitude similar to what is seen in Fig. 2.4.

The influence of the layer thickness non-uniformity on the defect mode amplitude is shown in Fig. 2.5. A comparison is made between the changes in the photonic bandgap amplitude in a photonic crystal without a defect and the defect mode amplitude in a photonic crystal with a defect with respect to layer thickness non-uniformity. The changes in amplitude are normalized to the maximum reflection of the photonic bandgap in the photonic crystal with no defect and ideal, abrupt, plane-parallel interfaces. The change in amplitude of the defect mode is more significant for increasing layer thickness non-uniformity compared to that for the photonic bandgap.

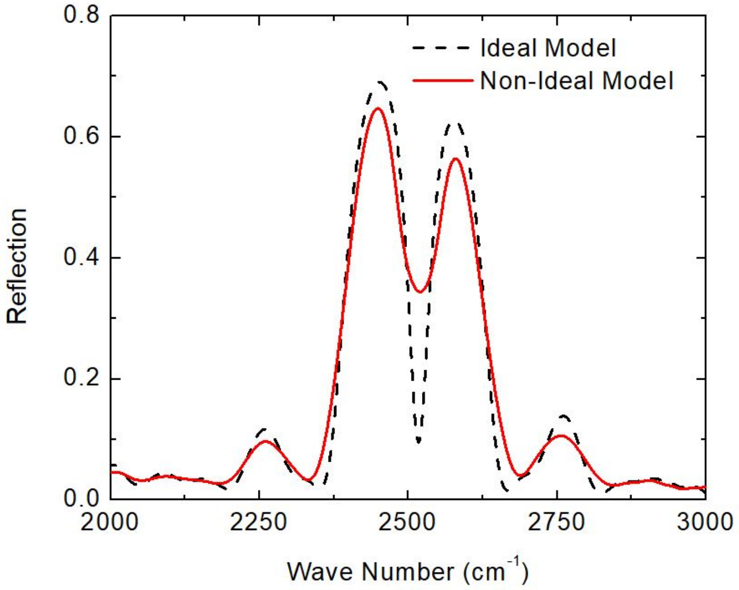

Figure 2.4: Model-calculated reflection data obtained for a stratified-layer model with ideal, plane parallel interfaces (black dashed line) in comparison to reflection data calculated using a model where a 2.8% layer thickness non-uniformity is assumed (red solid line). The largest difference can be observed at the defect mode resonance frequency, where the amplitude of the defect-mode is substantially suppressed after introducing layer thickness non-uniformity into the model.

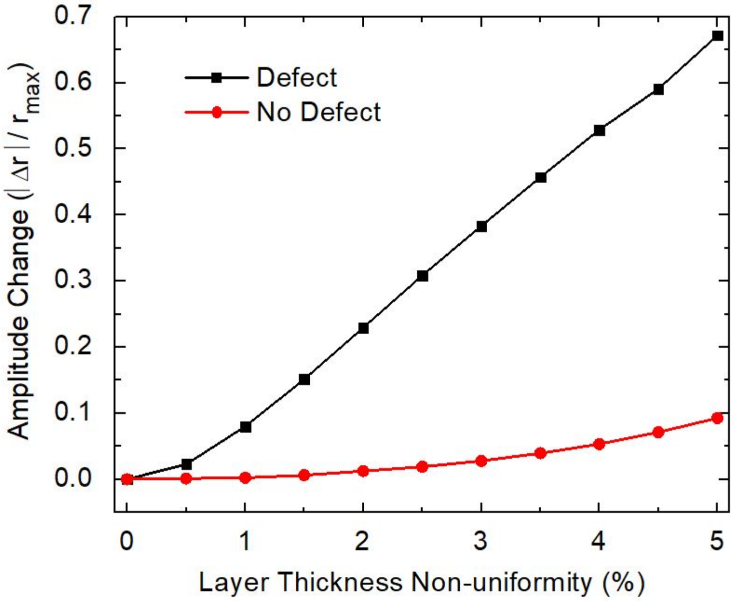

Figure 2.5: Amplitude change as a function of increasing layer thickness non-uniformity. The change in defect amplitude is more sensitive to changes in non-unifority between 0% and 5% where the bandgap amplitude of crystals without a defect experience only small changes in this range. Beyond 5% layer non-uniformity, the amplitude of the defect-mode is decreased to the point it is no longer observed.

This trend continues up to a non-uniformity of 5% at which point the defect mode becomes indistinguishable.

## 2.4 Conclusions

A one-dimensional photonic crystal with a solid, compact, defect layer was successfully fabricated by direct laser writing with two-photon polymerization. After determining and introducing one-dimensional geometric scaling factors for the low- and high-density layers, two photonic crystals were fabricated, identical except for the addition of a defect layer in one. For both crystals a photonic bandgap was identified experimentally. The photonic bandgap is centered at 2500 cm$^{-1}$. In the photonic crystal with a defect layer, a defect mode was induced in the middle of the the photonic bandgap.

Our stratified-layer optical model calculations are in a very good agreement with the experimental results. Best-model thickness values are in a very good agreement with the nominal design parameters. When the scaling factor ($\gamma_{\mathrm{SF}}$) was implemented, a stratified-layer optical analysis of the reflection data from these photonic crystals reveals best-model layer thicknesses within ±1.2% of our nominal design values. In introducing scaling factors, we take into account not only the voxel size, but the entire effect of the two-photon polymerization, rinsing, and drying process which results in the final geometry. Even minute changes in layer thickness non-uniformity had substantial effects on the amplitude of the defect mode. For the photonic bandgap these amplitude changes were not as pronounced. This sensitivity can be used to determine layer thickness non-uniformity in one-dimensional photonic crystals fabricated for the infrared spectral range by two-photon polymerization. The volumetric fill factor for the low-density layers was found to be 9.6% larger than designed. While having minimal effects on the shape of spectral features, this change resulted in a shift of the photonic bandgap from the designed 2556 $\mathrm{cm}^{-1}$ to 2500 $\mathrm{cm}^{-1}$. Note, that the scaling factor was omitted for the volumetric fill factor, which explains the substantial deviation of from its nominal value. This deviation may be reduced by introducing a separate scaling factor.

By introducing density dependent scaling factors in the design phase we have enabled the fabrication of one-dimensional photonic crystals with defect modes which have true-to-design layer thicknesses. In contrast to determining the layer thicknesses, the interface roughness (layer thickness non-uniformity) is difficult to assess. Therefore, one-dimensional photonic crystals engineered with narrow band defect modes may provide a method to quantify this important fabrication parameter. One-dimensional photonic crystals with defect modes demonstrate features relevant for applications as narrow band filters [20]. In addition, photonic crystals show promise as enhanced Faraday rotators [4], omnidirectional bandgap filters [5], and sensors [18, 19].

# REFERENCES

[1] E. Yablonovitch, “Inhibited spontaneous emission in solid-state physics and electronics,” *Phys. Rev. Lett.* **58**, 2059 (1987).

[2] S. John, “Strong localization of photons in certain disordered dielectric superlattices,” *Phys. Rev. Lett.* **58**, 2486 (1987).

[3] T. Hattori, N. Tsurumachi, and H. Nakatsuka, “Analysis of optical nonlinearity by defect states in one-dimensional photonic crystals,” *JOSA B* **14**, 348 (1997).

[4] M. Steel, M. Levy, and R. Osgood, “High transmission enhanced Faraday rotation in one-dimensional photonic crystals with defects,” *IEEE Photonic Tech. L.* **12**, 1171 (2000).

[5] H. Jiang, H. Chen, H. Li, Y. Zhang, and S. Zhu, “Omnidirectional gap and defect mode of one-dimensional photonic crystals containing negative-index materials,” *Appl. Phys. Lett.* **83**, 5386 (2003).

[6] H.-Y. Lee and T. Yao, “Design and evaluation of omnidirectional one-dimensional photonic crystals,” *J. Appl. Phys.* **93**, 819 (2003).

[7] C.-J. Wu and Z.-H. Wang, “Properties of defect modes in one-dimensional photonic crystals,” *Pr. Electromagn. Res.* **103**, 169 (2010).

[8] V. A. Tolmachev, A. V. Baldycheva, K. Berwick, and T. S. Perova, “Influence of fluctuations of the geometrical parameters on the photonic band gaps in one-dimensional photonic crystals,” *Pr. Electromagn. Res.* **126**, 285 (2012).

[9] M. V. Rybin, I. I. Shishkin, K. B. Samusev, P. A. Belov, Y. S. Kivshar, R. V. Kiyan, *et al.*, “Band structure of photonic crystals fabricated by two-photon polymerization,” *Crystals* **5**, 61 (2015).

[10] H. Shen, Z. Wang, Y. Wu, and B. Yang, "One-dimensional photonic crystals: fabrication, responsiveness and emerging applications in 3D construction," *RSC Adv.* **6**, 4505 (2016).

[11] Y. Li, D. Fullager, S. Park, D. Childers, R. Fesperman, G. Boreman, and T. Hofmann, "High-contrast infrared polymer photonic crystals fabricated by direct laser writing," *Opt. Lett.* **43**, 4711 (2018).

[12] S. Park, Y. Li, B. Norton, M. McLamb, G. D. Boreman, and T. Hofmann, "One-dimensional Photonic Crystals Fabricated Using Stereolithographic Single Layer Assembly for the Terahertz Spectral Range," *J. Infrared Millim. Te.* **41**, 542 (2020).

[13] S. Park, Y. Li, M. McLamb, B. Norton, G. D. Boreman, and T. Hofmann, "Highly Localized Defect Mode in Polymer-Based THz Photonic Crystals Fabricated Using Stereolithography," *J. Infrared Millim. Te.* **41**, 825 (2020).

[14] A. Sánchez, A. Porta, and S. Orozco, "Photonic band-gap and defect modes of a one-dimensional photonic crystal under localized compression," *J. Appl. Phys.* **121**, 173101 (2017).

[15] A. M. Ahmed, H. A. Elsayed, and A. Mehaney, "High-Performance Temperature Sensor Based on One-dimensional Pyroelectric Photonic Crystals Comprising Tamm/Fano Resonances," *Plasmonics* **16**, 547 (2021).

[16] E. Yablonovitch, "Photonic crystals," *J. Mod. Optic.* **41**, 173 (1994).

[17] A. H. Aly and H. A. Elsayed, "Defect mode properties in a one-dimensional photonic crystal," *Physica B* **407**, 120 (2012).

[18] B.-F. Wan, Z.-W. Zhou, Y. Xu, and H.-F. Zhang, "A theoretical proposal for a

refractive index and angle sensor based on one-dimensional photonic crystals," *IEEE Sensors Journal* **21**, 331 (2020).

[19] R. Nelson and J. Haus, "One-dimensional photonic crystals in reflection geometry for optical applications," *Appl. Phys. Lett.* **83**, 1089 (2003).

[20] A. H. Aly, H. A. Elsayed, and C. Malek, "Defect modes properties in one-dimensional photonic crystals employing a superconducting nanocomposite material," *Opt. Appl.* **48**, 53 (2018).

[21] F. Scotognella, A. Chiasera, L. Criante, E. Aluicio-Sarduy, S. Varas, S. Pelli, *et al.*, "Metal oxide one dimensional photonic crystals made by RF sputtering and spin coating," *Ceram. Int.* **41**, 8655 (2015).

[22] R. Langer, A. Barski, J. Simon, N. Pelekanos, O. Konovalov, R. Andre, and L. S. Dang, "High-reflectivity GaN/GaAlN Bragg mirrors at blue/green wavelengths grown by molecular beam epitaxy," *Appl. Phys. Lett.* **74**, 3610 (1999).

[23] R. Houbertz, P. Declerck, S. Passinger, A. Ovsianikov, J. Serbin, and B. Chichkov, "Investigations on the generation of photonic crystals using two-photon polymerization (2PP) of inorganic–organic hybrid polymers with ultra-short laser pulses," *Phys. Status Solidi A.* **204**, 3662 (2007).

[24] H. Jee, M.-J. Park, K. Jeon, C. Jeong, and J. Lee, "Combining Interference Lithography and Two-Photon Lithography for Fabricating Large-Area Photonic Crystal Structures with Controlled Defects," *Appl. Sci.* **11**, 6559 (2021).

[25] J.-F. Xing, M.-L. Zheng, and X.-M. Duan, "Two-photon polymerization microfabrication of hydrogels: an advanced 3D printing technology for tissue engineering and drug delivery," *Chem. Soc. Rev.* **44**, 5031 (2015).

[26] D. Tan, Y. Li, F. Qi, H. Yang, Q. Gong, X. Dong, and X. Duan, "Reduction in feature size of two-photon polymerization using SCR500," *Appl. Phys. Lett.* **90**, 071106 (2007).

[27] Y.-L. Zhang, Q.-D. Chen, H. Xia, and H.-B. Sun, "Designable 3D nanofabrication by femtosecond laser direct writing," *Nano Today* **5**, 435 (2010).

[28] K. S. Worthington, L. A. Wiley, E. E. Kaalberg, M. M. Collins, R. F. Mullins, E. M. Stone, and B. A. Tucker, "Two-photon polymerization for production of human iPSC-derived retinal cell grafts," *Acta Biomater.* **55**, 385 (2017).

[29] D. B. Fullager, G. D. Boreman, and T. Hofmann, "Infrared dielectric response of nanoscribe IP-dip and IP-L monomers after polymerization from 250 $\text{cm}^{-1}$ to 6000 $\text{cm}^{-1}$," *Opt. Mater. Express* **7**, 888 (2017).

[30] W. Cai and V. M. Shalaev, *Optical metamaterials*, vol. 10, Springer, (2010).

[31] Y. Li, D. Fullager, E. Angelbello, D. Childers, G. Boreman, and T. Hofmann, "Broadband near-infrared antireflection coatings fabricated by three-dimensional direct laser writing," *Opt. Lett.* **43**, 239 (2018).

# CHAPTER 3: MECHANICALLY TUNABLE PHOTONIC CRYSTALS

## 3.1 Mechanical Control of the Optical Bandgap in One-Dimensional Photonic Crystals

Over the last several years, two-photon polymerization has been a popular fabrication approach for photonic crystals due to its high spatial resolution.[1] One-dimensional photonic crystals with photonic bandgap reflectivities over 90% have been demonstrated for the infrared spectral range. With the success of these structures, methods which can provide tunability of the photonic bandgap are being explored. In this study, we demonstrate the use of mechanical flexures in the design of one-dimensional photonic crystals fabricated by two-photon polymerization for the first time. Experimental results show that these photonic crystals provide active mechanically induced spectral control of the photonic bandgap. An analysis of the mechanical behavior of the photonic crystal is presented and elastic behavior is observed. These results suggest that one-dimensional photonic crystals with mechanical flexures can successfully function as opto-mechanical structures.

### 3.1.1 Introduction

Photonic crystals have been explored for photonic bandgap filtering applications over the last several decades [1–6]. This is due to their ability to provide nearly perfect reflection within narrow bandgaps which can function over a broad spectral range. These spectral regions with high reflectivities and little to no transmission are known as photonic bandgaps. Photonic crystals induce a photonic bandgap by

---

[1] Reprinted with permission from V. P. Stinson, N. Shuchi, M. McLamb, G. D. Boreman, and T. Hofmann, "Mechanical Control of the Optical Bandgap in One-Dimensional Photonic Crystals," *Micromachines* **13**, 2248 (2022). © 2022, MDPI.

creating a dielectric periodicity in either one-, two-, or three-dimensions [5]. In the one-dimensional case, this periodicity is created along a single axis [1, 2, 7–12].

There are several effective fabrication approaches for one-dimensional photonic crystals such as spin coating, self-assembly, chemical/physical vapor deposition, top-down etching, and molecular beam epitaxy [13, 14]. While these approaches each have their advantages, they are restricted in terms of geometrical design freedom. A recent approach in the fabrication of one-dimensional photonic crystals is direct laser writing by two-photon polymerization [11, 15–17]. This approach allows for the fabrication of complex geometrical structures on a scale which is sub-wavelength for most infrared applications [18, 19]. With the aforementioned fabrication approaches, at least two dielectric materials must be used in order to form the necessary dielectric periodicity. In direct laser writing, dielectric periodicity can be produced using a single dielectric material by varying the density of the layers [11, 17].

While the highly reflective photonic bandgaps are in themselves extremely useful spectral features, many researchers have looked to provide even further spectral control by mechanical means [6, 12, 20, 21]. Many of these studies explore the ability to control spectral features produced by photonic crystals by mechanically straining the material [20–22]. For the one-dimensional photonic crystal, the photonic bandgap is extremely sensitive to changes in layer thickness. By introducing layers containing mechanically flexible constituents [23, 24] a mechanical force can be used to either expand or compress the photonic crystal. This will allow the active control of the photonic bandgap by mechanical stimuli. This concept has been demonstrated in the THz spectral range by implementing cantilevers into the one-dimensional photonic crystal design [23].

In this study, we present a one-dimensional photonic crystal design which allows mechanically induced spectral tuning of the photonic bandgap in the infrared spectral range for the first time. To accomplish this, a bow tie flexure design adapted from Ref. 24 is scaled down such that the dimensions are subwavelength for the spectral range of interest in this study. Experimental results suggest that these one-dimensional photonic crystals with flexures fabricated by two-photon polymerization exhibit mechanical hysteresis while in compression, as expected of an elastic material [25]. The results reported here suggest that one-dimensional photonic crystals with flexures fabricated by two-photon polymerization may be used in novel opto-mechanical devices enabling mechanical tuning of optical features.

### 3.1.2 Design, Fabrication, and Characterization

The one-dimensional photonic crystals under study were designed using a stratified-layer optical model (WVASE32, J.A. Woollam, Co., Lincoln, NE, USA) in combination with a mechanical finite-element model (COMSOL, Multiphysics). A single photo-sensitive polymer (IP-Dip) was used to fabricate the one-dimensional photonic crystal. The mechanical properties for IP-Dip vary widely depending on fabrication parameters, the properties which were employed during finite-element modeling were obtained from Refs [26, 27]. To induce dielectric periodicity using a single polymer, 13 plane parallel layers of alternating high- and low-density were used (see Figure 3.1). The dielectric properties of the compact, high-density, layers have been previously established using spectroscopic ellipsometry in the infrared spectral range and are described using a simple mixed oscillator model [28]. The low-density layers consist of the printed mechanical flexures and the void (air) between adjacent flexures. The dielectric properties of these layers are calculated using the Bruggeman effective medium approximation [29]. The use of this approximation to model the spectral response of one-dimensional photonic crystals is described in detail in previous publications [7, 11, 17, 23, 30].

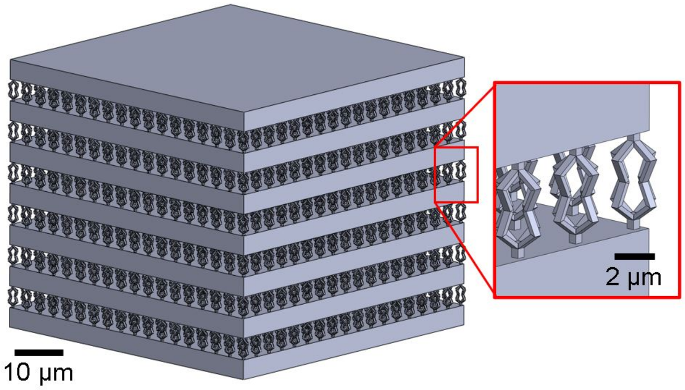

Figure 3.1: Computer-aided model of the designed one-dimensional photonic crystal investigated here. The photonic crystal consists of alternating high-density compact and low-density layers. The nominal thickness of the high-density layers is 3.35 µm. The low-density layers with a nominal thickness of 3.40 µm are composed of an array of bow tie flexures which are arranged in a square-lattice pattern on the surface with a lattice constant of 2.85 µm. The corresponding nominal volumetric fill factor $f_i$ of the low-density layer is $f_i = 0.04$.

To demonstrate the ability of the designed photonic crystals to produce spectral bandgap shifts upon compression, the layer thickness and dielectric composition of the low-density layers were designed such that several bandgaps were induced within the measurement window (1000–5000 cm$^{-1}$). Within this region, the initial bandgap is induced at 2000 cm$^{-1}$ and the final at 4700 cm$^{-1}$. This spectral range was selected based on the dielectric function of IP-Dip which offers a transparent window from 1800 to 5000 cm$^{-1}$ [28]. The high-density layer thickness was designed to be 3.35 µm. The low-density layer thickness was designed to be 3.40 µm. Each low-density layer consists of an 18 × 18 array of bow tie flexures, arranged in a square lattice pattern with a periodicity of 2.85 µm. The base of the one-dimensional photonic crystal is 49.2 µm × 49.2 µm. The computer-aided design for the resulting geometry can be seen in Figure 3.1.

A commercially available two-photon polymerization system (Photonic Professional GT, Nanoscribe, GmBH) was employed in the fabrication of these one-dimensional photonic crystals from a single photosensitive monomer (IP-Dip). The selection of appropriate print parameters is essential in order to produce a sample which is true to design. The designed bow tie flexures push the resolution limits of this system, limiting the range of print parameters which can successfully produce a given geometry. Many print parameters such as the choice of objective, monomer, laser power, scan speed, and hatching and slicing distance will affect the voxel size of the system [31–34]. The voxel is the ellipsoidal volume in which there is enough photon irradiance to polymerize the monomer. To efficiently determine the best settings for this geometry, a dose matrix was performed in which several combinations of scan speed and laser power were tested. Here the 63x objective was chosen with both hatching and slicing distances set to 0.2 µm. A single low-density layer was printed on top of a high-density layer. Scanning electron microscope images were taken in order to compare the quality. Scan speeds ranging from 500 to 5000 mm/s were tested with laser powers ranging from 20 to 50% of the maximum output power of 25 kW.

The scanning electron microscope images for the two best scan speed and laser power combinations can be seen in Figure 3.2. From the top down view given by (b) and (d), it appears that the 50% laser power resulted in the best geometry compared with the 20% layer. However, upon taking a side view of these layers at a higher magnification it can be seen that the layer fabricated at 50% laser power (a) has been over-polymerized compared to the layer fabricated at 20% laser power (c). In order to ensure a hollow center within the flexures, a lower laser power must be used. There is an apparent compromise in structural stability as laser power is decreased, which can be seen in the collapse of flexures in (d) compared to the stable flexures in (b). However, when fabricating the complete one-dimensional photonic crystal, this behavior is not an issue because the high-density layers provide the necessary permanence to maintain an upright orientation. Thus, a scan speed of 500 mm/s and laser power of 20% was chosen for the fabrication of the complete photonic crystal.

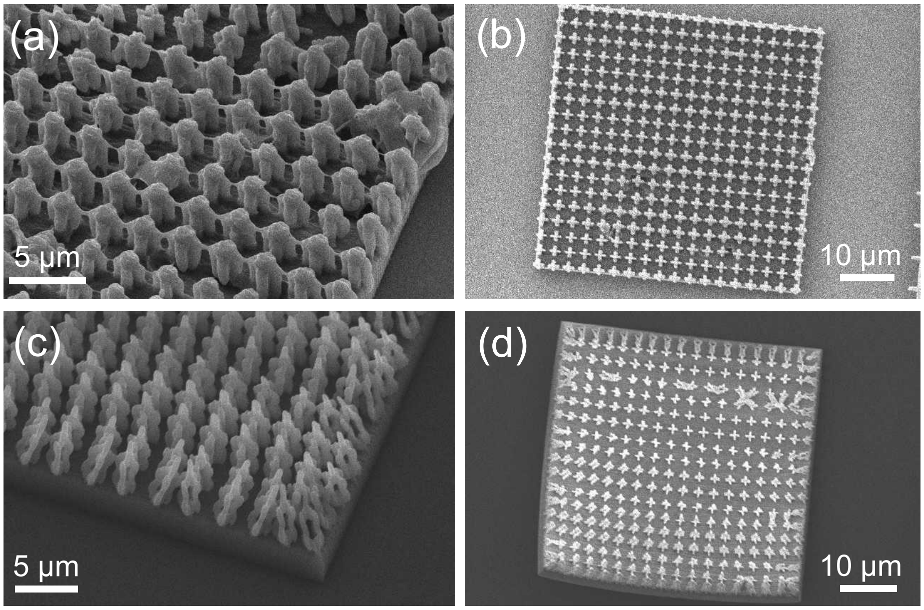

Figure 3.2: Scanning electron microscope images of single flexure layers which were fabricated with different laser power settings. Images (a) and (b) show two views of a flexure layer which was fabricated using 500 mm/s scan speed with 50% laser power. Images (c) and (d) show the same views of a layer fabricated using 500 mm/s scan speed with 20% laser power.

A 4 × 4 array of one-dimensional photonic crystals with 3 mm square lattice periodicity were fabricated on a fused silica substrate. This arrangement was chosen based on finite-element model calculations of the elastic properties of the bow tie flexure design. Compressive force was applied to the photonic crystals in increments. In order to provide an even distribution of pressure while maintaining transparency for measurement, a fused silica window with thickness 0.7 mm was placed on the array. This window was measured to have a mass of 1.37 g. Subsequent slides were placed on top of the initial window in log-cabin style to provide incremental increases in compressive force without interfering with the central measurement aperture. These subsequent increases in loading were done in steps of 2.83 g.

Infrared reflection measurements were taken of the photonic crystal for the spectral range from 1000 $\text{cm}^{-1}$ to 5000 $\text{cm}^{-1}$ with resolution 2 $\text{cm}^{-1}$. An IR microscope (HYPERION 3000 Bruker, Inc., Billerica, MA, USA) with a Fourier-transform infrared spectrometer (VERTEX 70, Bruker, Inc., Billerica, MA, USA) was used for these measurements. This system uses a silicon carbide globar as the infrared light source. A 15× cassegrain objective with a square aperture of 20 μm × 20 μm was selected, resulting in an angular spread of 0.6° with an average angle of incidence of 8.7°. All measurements were normalized to the reflection of a bulk gold sample using identical parameters to those aforementioned. Experimental measurements were taken at room temperature.

### 3.1.3 Results and Discussion

In order to determine which photonic bandgaps were appropriate to observe upon compression, two Fourier-transform infrared reflection measurements were taken of the photonic crystal both with and without the presence of the fused silica window. Here kapton tape spacers are placed around around the edges of the fused silica window in order to prevent compression, allowing the effects of the fused silica window on the photonic bandgaps to be isolated. These measurements are given in Figure 3.3. The red dashed curve shows the measurements for the photonic crystal in air where four distinct photonic bandgaps can be seen. The black dashed curve shows the measurements where the fused silica window has been introduced but is not yet in contact with the structures. From this comparison, it is apparent that three of the four photonic bandgaps induced within this spectral range experience minimal amplitude loss due to the fused silica window. Thus, the photonic bandgap centered at 4040 $\text{cm}^{-1}$ was chosen to observe due to its amplitude and position within the measurement window.

The experimental reflection data for two compressive cycles are given in Figure 3.4 where the measurement window is centered around the 4040 $\text{cm}^{-1}$ bandgap. For the first point in the compressive cycle shown in Figure 3.4 (b) and (d), the peak shift is 0 $\text{cm}^{-1}$. The reflection spectra for these initial points in the load curve can be seen in Figure 3.4 (a) and 3.4 (c), respectively, for F = 0.84 mN. For each point in (b), as the photonic crystal is loaded and unloaded, the peak center is measured from (a) and the peak shift is recorded in (b) as a function of compressive force. The same process is followed for the second cycle given in (c) and (d). For visual clarity, each subsequent curve in (a) is vertically offset by 0.5 relative reflection intensity. During these cycles, the rate of shift is higher during loading than unloading. Comparing the photonic bandgaps during this cycle in (a) it is clear the peak center does not return to the initial position even though it is under the same compressive force. During the second compressive cycle, the maximum compressive force is increased from 4.31 mN per photonic crystal to 6.05 mN. While the degree of shifting varies between cycles, the general shape of the curves is similar (see Figure 3.4 (b) and (d)). Peak shifting to larger wavenumbers during loading aligns with the expected effects of reducing the low-density layer thickness. Similarly, shifting to smaller wavenumbers during unloading is expected as low-density layer thickness is increased.

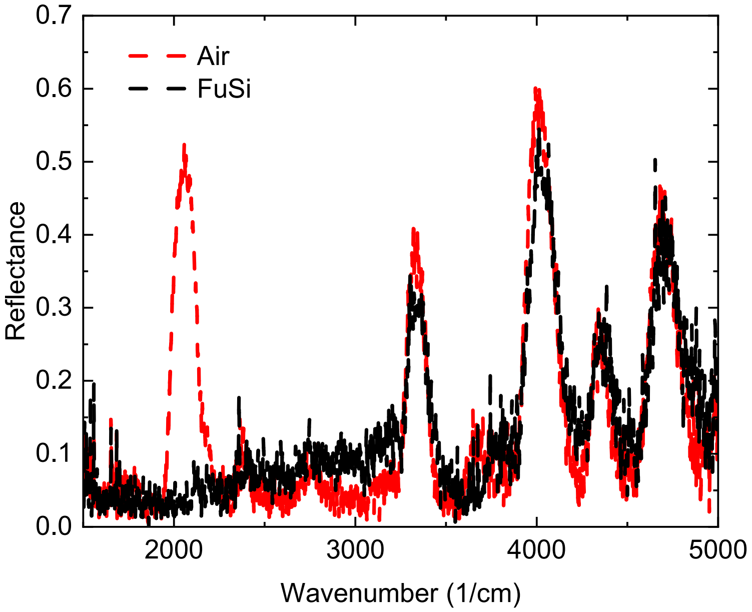

Figure 3.3: Fourier-transform infrared reflection measurements of the fabricated photonic crystal measured both in air (black dashed) and through a Fused Silica substrate (red dashed). At this stage, there is no compression on the photonic crystal.

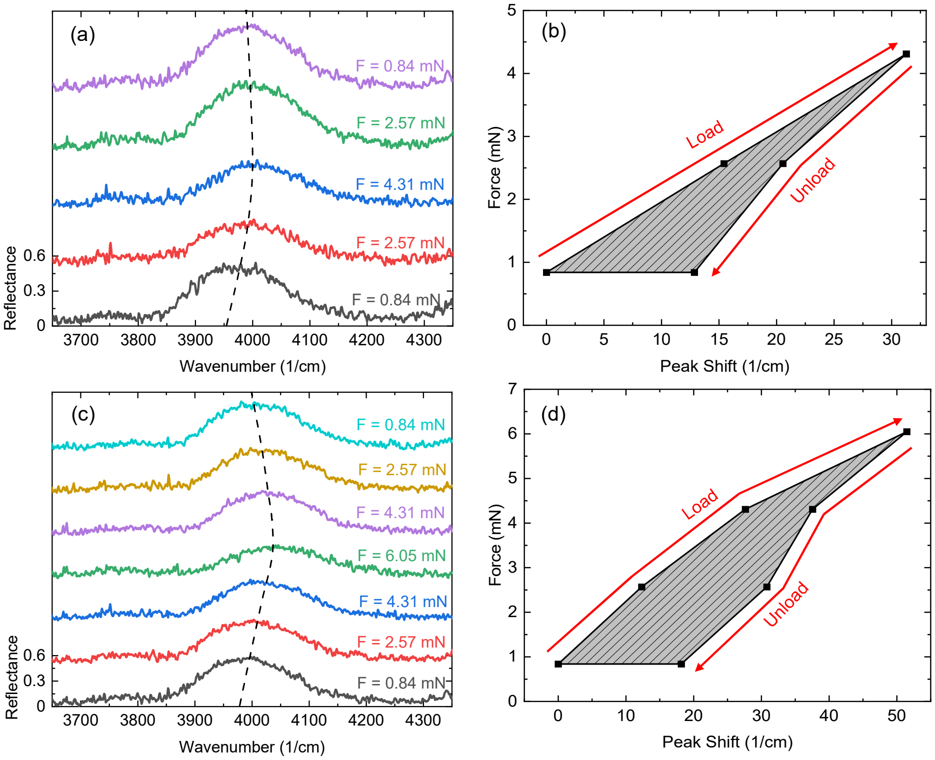

Figure 3.4: Effect of compressive force on photonic bandgap spectral positioning and amplitude for two cycles. Here the photonic bandgap centered at 4040 cm$^{-1}$ in Figure 3.3 is isolated and studied. The Fourier-transform infrared reflection measurements for this bandgap are given in (a) and (c) for loading and unloading where a shift of the peak center can be seen as well as fluctuations in amplitude. An offset of 0.5 relative reflection intensity is introduced between adjacent curves for visualization. A mechanical hysteresis curve following the compressive cycles of (a) and (c) is plotted in (b) and (d), respectively. Here compressive force is plotted as a function of shift in peak center.

### 3.1.4 Conclusions

One-dimensional photonic crystals with mechanical flexures fabricated by two-photon polymerization have demonstrated spectral shifting as a function of compressive force. The photonic crystal consists of 13 alternating layers of high- and low-density. The ability of such a device to induce high-contrast photonic bandgaps in the infrared spectral range has been demonstrated previously [11, 17]. In this study, mechanical flexure arrays are implemented to function as the low-density layers. Due to the photonic bandgap's sensitivity to changes in layer thickness, compression of the photonic crystal induces spectral shifting of the photonic bandgaps which can be observed in Figure 3.4. Such an effect has been previously demonstrated in the THz spectral range using stereo-lithography [23]. In contrast to the previous THz demonstration, the low-density layer geometry was altered in this study to include vertically symmetric flexure arrays as opposed to cantilevers arrays. When comparing compressive effects on the photonic bandgap observed in this study with the THz demonstration, it appears that the effects on bandgap amplitude and broadening during compression are reduced.

In conclusion, a mechanically tunable one-dimensional photonic crystal designed for the infrared spectral range was fabricated using two-photon polymerization. The elastic capabilities of this device were tested by conducting loading and unloading cycles. During cycles, Fourier-transform infrared reflection measurements were taken to observe the effect of compressive force on the photonic bandgap's spectral location and amplitude. The results of this study suggest one-dimensional photonic crystals with mechanical flexures allow dynamic control of spectral features by way of mechanical stimuli. While static one-dimensional photonic crystals have clear applications in sensing and bandgap filtering, the addition of mechanical tunability opens doors for uses in fields such as micro-robotics and micro-optomechanical systems (MOEMS) [35].

## 3.2 Photonic Crystals Fabricated by Two-Photon Polymerization with Mechanical Defects

One-dimensional photonic crystals have been used in sensing applications for decades, due to their ability to induce highly reflective photonic bandgaps.[2] In this study, one-dimensional photonic crystals with alternating low- and high-density layers were fabricated from a single photosensitive polymer (IP-Dip) by two-photon polymerization. The photonic crystals were modified to include a central defect layer with different elastic properties compared to the surrounding layers, for the first time. It was observed that the defect mode resonance can be controlled by compressive force. Very good agreement was found between the experimentally measured spectra and the model data. The mechanical properties of the flexure design used in the defect layer were calculated. The calculated spring constant is of similar magnitude to those reported for microsprings fabricated on this scale using two-photon polymerization. The results of this study demonstrate the successful control of a defect resonance in one-dimensional photonic crystals fabricated by two-photon polymerization by mechanical stimuli, for the first time. Such a structure could have applications in fields, such as micro-robotics, and in micro-opto–electro–mechanical systems (MOEMS), where optical sensing of mechanical fluctuations is desired.

### 3.2.1 Introduction

Photonic crystals have been of interest in sensing applications for several decades [1, 13, 36]. This attention can be attributed to the photonic bandgaps found in photonic crystals. These photonic bandgaps create spectral regions of high reflectivity with little to no transmission [9, 13, 37]. Photonic crystals are generally categorized, based on their periodic arrangement, as being one-, two-, or three-dimensional [5, 36]. For

---

[2] Reprinted with permission from V. P. Stinson, N. Shuchi, D. Louisos, M. McLamb, G. D. Boreman, and T. Hofmann, "Photonic Crystals Fabricated by Two-Photon Polymerization with Mechanical Defects," *Optics* **4**, 300 (2023). © 2023, MDPI.

the purpose of this study we focus on the one-dimensional photonic crystal geometry where dielectric periodicity is created along a single axis [1, 2, 7–12].

In order to create the necessary dielectric contrast between layers to induce photonic bandgaps, different materials are generally used. Often spin coating is used to deposit series of thin films with carefully controlled thicknesses [13, 38]. Alternative methods, such as self-assembly, chemical vapor deposition, physical vapor deposition, and molecular beam epitaxy, are also well established [13, 14]. While these fabrication approaches have a clear advantage in their scalability, they are restricted in terms of geometric freedom. Recently, a direct laser writing approach, two-photon polymerization, was used to fabricate one-dimensional photonic crystals [11, 15–17, 39]. When compared with conventional techniques, this approach allows more design flexibility.

In this study, one-dimensional photonic crystals are fabricated from a single dielectric material by two-photon polymerization. As opposed to creating the necessary dielectric contrast by altering materials, contrast is created by varying the density between layers. This method of using density-dependent layers to fabricate high-contrast photonic crystals has been successfully demonstrated in the infrared and terahertz spectral ranges [7, 11, 17, 23, 30].

While the highly reflective photonic bandgap is, in itself, a versatile feature for spectral-filtering applications, it is possible to add additional spectral control by disrupting the spatial or dielectric periodicity of the photonic crystal. Such defects can be designed so that narrow transmission bands may exist within the otherwise reflective photonic bandgap. The ability to induce these narrow defect transmission bands has been well documented [1, 2, 8, 12, 30, 40–42]. The applications for one-dimensional photonic crystals with defects range from sensors [3, 4] and narrow-band filters [5] to more complex devices, such as enhanced Faraday rotators [1] and omnidirectional bandgap filters [2].

The spectral capabilities of photonic crystals can be taken a step further through mechanical manipulation. Studies involving the structural alteration of photonic crystals by mechanical stimuli have increased in recent years [6, 12, 20, 21]. Many of these investigations demonstrate that the photonic crystal's spectral features may be controlled by mechanically straining the structure [20–22]. In the one-dimensional photonic crystal case, spectral features have an innate sensitivity to changes in geometric parameters such as layer thickness. Exploiting this sensitivity, one-dimensional photonic crystals can be designed such that the layers consist of mechanically flexible constituents and, thus, the layer thickness can be mechanically varied. Such configurations in one-dimensional photonic crystals have been used to control layer thicknesses by mechanical force [23, 24, 39].

The use of photonics for mechanical sensing is a growing and well established field. Depending on the desired sensitivity, several system designs have proven to be effective. Three designs which have been of particular interest in mechanical sensing are Mach–Zehnder interferometers [43, 44], photonic micro-electromechanical systems [45–47], and fibre bragg gratings [48]. Using these methods, the ability to sense small mechanical changes ranges from highly sensitive, in the order of 12 pm/MPa [46], to relatively insensitive, in the order of 0.2 pm/Pa [44]. Applications for devices which provide photonic mechanical sensing range from MOEMS [35, 45] to more sophisticated systems, such as micro-robotics [35] and internal biological–pressure sensing [49].

Initial demonstrations of the ability of one-dimensional photonic crystals composed of high- and low-density layers to combine optical and mechanical capabilities were designed for the terahertz spectral range. These one-dimensional photonic crystals were fabricated by stereo-lithography. With success in the fabrication of high-contrast one-dimensional photonic crystals [7], the ability to induce defect resonances by introducing a centralized defect layer was investigated [30]. Following these studies, active mechanical tuning of the photonic bandgap was realized by introducing cantilever arrays to the low-density layers. As a function of compressive force, the photonic bandgap experienced spectral shifting [23]. Combining concepts from these studies, a central air-gap defect layer was designed such that the defect layer thickness could be mechanically controlled. By varying the thickness of this defect layer, tuning of the defect resonance within the photonic bandgap was demonstrated for the first time [50].

Many of these same concepts have been demonstrated in the infrared spectral range using two-photon polymerization [11, 17, 39]. We previously demonstrated the ability to induce narrow transmission bands produced by defect resonances in reflective photonic bandgaps [17]. Recently, we showed the ability to allow dynamic spectral control of the photonic bandgap by introducing mechanical flexures in the low-density layers of the photonic crystal [39]. Inspired by the terahertz demonstration (Ref. 50), the purpose of this study was to combine these concepts to create a one-dimensional photonic crystal for the infrared spectral range, whose transmissive defect resonance within the reflective bandgap can be mechanically tuned. By introducing a centralized defect layer, composed of an array of sub-wavelength mechanical flexures, the spectral location of a defect resonance was controlled by compressive force. This opto-mechanical sensitivity may prove useful in applications, such as those in MOEMS and micro-robotics [35].

As science advances, there is a persistent need to miniaturize in order to provide more functionality without increasing the size of the system. As a result, two photon polymerization has become a popular approach for the development of micro-actuators [51]. Devices fabricated using this process have demonstrated the ability to provide a mechanical action as a function of external stimuli. There are many methods of stimulation which are being explored for actuation. A few which have recently been realized experimentally include electro-magnetic and chemical stimulation [35, 52–54]. The development of actuating devices on the micro-scale is an essential step to fulfilling the demands of future technology.

### 3.2.2 Design, Fabrication, and Characterization

A simple stratified layer optical model (WVASE32, J.A. Woolam, Co., Lincoln, NE, USA) was employed to design the one-dimensional photonic crystal. This model calculates the spectral response of a given stratified layer design using the Fresnel equations in conjunction with thin film interference expressions. The photonic crystal is modeled as a stack of three dielectrics. These dielectrics are termed the high-density, low-density and defect layers. The permittivity of the high-density layers, which are composed entirely of a resin compatible with two-photon polymerization (IP-Dip), were taken from Ref. 28. The permittivity for both the low-density layers and defect layer, as shown in Figure 3.5, were calculated using the Bruggeman effective medium approximation given by [29]:

$$\begin{aligned} \varepsilon^{\mathrm{eff}}(\omega, f_{\mathrm{i}}) &= \frac{1}{4}\Big\{(3f_{\mathrm{i}}-1)\varepsilon_{\mathrm{i}}(\omega)+(2-3f_{\mathrm{i}})\varepsilon_{\mathrm{h}}(\omega) \pm \\ &\quad \Big([(3f_{\mathrm{i}}-1)\varepsilon_{\mathrm{i}}(\omega)+(2-3f_{\mathrm{i}})\varepsilon_{\mathrm{h}}(\omega)]^2+\varepsilon_{\mathrm{i}}(\omega)\varepsilon_{\mathrm{h}}(\omega)\Big)^{\frac{1}{2}}\Big\}. \end{aligned} \tag{3.1}$$

In this approximation, the effective permittivity for the low-density layers is calculated using the properties of the inclusions $\varepsilon_{\mathrm{i}}$ and host medium $\varepsilon_{\mathrm{h}}$. In this design, the inclusions are composed of the same photosensitive polymer (IP-Dip) as the high-density layers $\varepsilon_{\mathrm{i}}(\omega) = \varepsilon_{\mathrm{IP-Dip}}(\omega)$. The host medium in this case is air $\varepsilon_{\mathrm{h}} = 1$. The volumetric fill factor $f_i$ describes the spatial ratio of inclusions to host medium within these layers. For this approximation to accurately describe the dielectric response of the low-density and defect layers, it is essential that the geometric features within these layers be sub-wavelength.

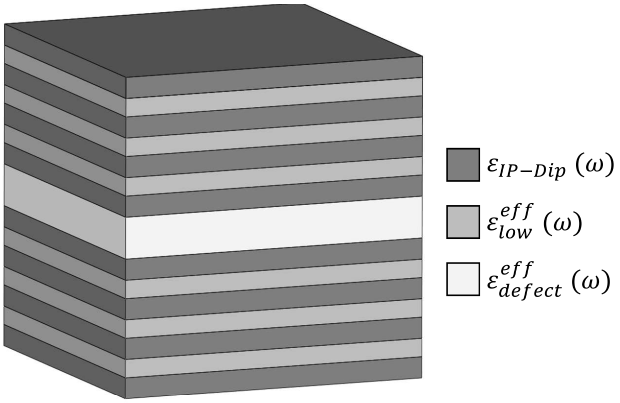

Figure 3.5: The spatial layer arrangements and layer permittivities used to model the optical response of the designed photonic crystal can be seen. Permittivities with the superscript "*eff*" are calculated using the Bruggeman effective medium approximation given in Equation (3.1). The permittivity with a subscript "*IP-Dip*" is used for the high-density layers which are composed entirely of the photosensitive polymer used in this study.

A geometry was designed such that a photonic bandgap was induced at $\omega = 2500$ cm$^{-1}$ ($\lambda = 4$ µm), and was, thus, centered in a transparent region for IP-Dip [28]. This geometry can be seen in Figure 3.6. The designed photonic crystal is composed of 14 alternating layers of high- and low-density with a centralized mechanical defect layer. The nominal thickness of the high-density and low-density layers are 3.35 µm and 2.92 µm, respectively. The low-density layers are composed of an array of sub-wavelength pillars, each with a diameter of 1.20 µm. The pillars are arranged in a square lattice with periodicity of 2.40 µm. The thickness of the defect layer is 6.63 µm. It consists of an array of bow-tie flexures, similar to those shown in Ref. 24, arranged in a square lattice with periodicity of 2.85 µm. Based on these geometries, the volumetric fill factor for the low-density and defect layers were calculated as $f_i = 0.20$ and $f_i = 0.02$, respectively. The square base of the photonic crystal is 49.2 µm × 49.2 µm.

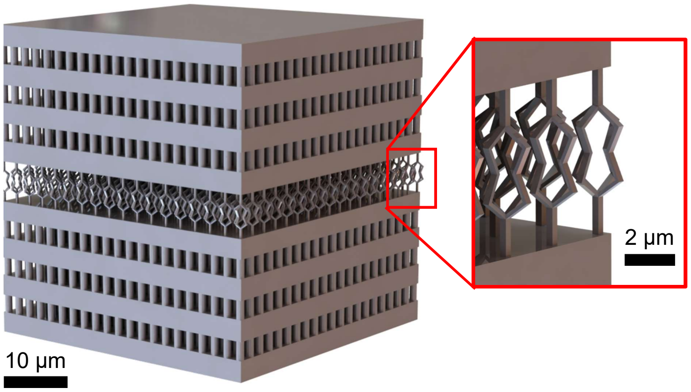

Figure 3.6: CAD model of the designed one-dimensional photonic crystal under study. The photonic crystal is composed of 14 alternating layers of high- and low-density with a centralized mechanical defect layer. The nominal thicknesses of the high-density, low-density, and defect layers were modeled to be 3.35 µm, 2.92 µm, and 6.63 µm, respectively.

The designed one-dimensional photonic crystal was fabricated using a commercially available two-photon polymerization system (Photonic Professional GT, Nanoscribe, GmbH, Karlsruhe, Germany). Using this system, the photonic crystal was polymerized on a fused silica substrate. The bow-tie flexures used in the defect layer approached the resolution limits of the two-photon polymerization system. Due to this, it was essential to isolate the bow-tie array to observe the effects of fabrication parameters on the resulting geometry. The optimization method followed in this study was discussed in detail in a previous study, where similar bow-tie flexures were designed for use in the low-density layers of photonic crystals [39].

A dose matrix was performed where scan speed and laser power were varied. Slicing and hatching distances, which define the space between consecutive laser scans, were kept constant at 0.2 µm. SEM images were taken of the dose matrix in order to assess quality. The settings which provided the best results for the flexure layer, as shown in Figure 3.2, were found to be at a 500 mm/s scan speed and 50% laser power (maximum 25 kW). It can be seen that, for these parameters, the central region of the bow-tie was hollow, allowing the array to flex as designed.

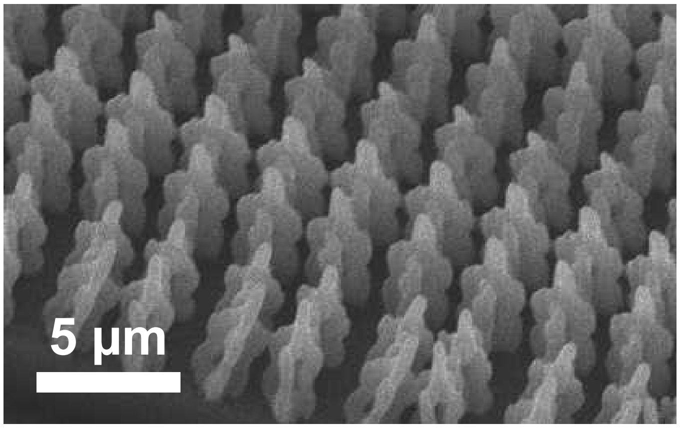

Figure 3.7: Scanning electron microscope image of an array of mechanical flexures. This array was fabricated with a scan speed of 500 mm/s at 50% laser power (max 25 kW). The periodic arrangement of this array matched that of the mechanical defect layer in Figure 3.6.

In order to correct for swelling and contraction effects, which occur during fabrication, scaling factors $\gamma_{\text{SF}}$ were applied to the desired nominal layer thicknesses. Conventionally, layer-specific print parameters would need to be used to nullify these effects. The scaling factor approach effectively compensates for the variation in volume-to-surface ratio between the high- and low-density layers without requiring the use of layer-specific print parameters. The scaling factors used for this study were previously determined and verified through SEM imaging [17]. The scaling factors for the high- and low-density layers were $\gamma_{\text{SF}} = 0.92$ and $\gamma_{\text{SF}} = 1.30$, respectively.

A transparent window of fused silica was selected to act as the compressive component, in order to provide transparency in the spectral region of the induced photonic bandgap, and, thus, allowing infrared reflection measurements during compression. A 4 × 4 array of the designed photonic crystal was fabricated on the substrate with a square lattice periodicity of 3 mm. Force was applied to the photonic crystals normal to the layer interfaces by placing the window material on the 4 × 4 photonic crystal array. The mass of the window was measured to be 1.37 g. Assuming a uniform force distribution, the applied force per photonic crystal of 0.84 mN was obtained.

Reflection measurements were taken in the infrared spectral range from 2000 $\text{cm}^{-1}$

(5.00 µm) to 3000 cm$^{-1}$ (3.33 µm), with resolution of 2 cm$^{-1}$. A HYPERION 3000 infrared microscope (Bruker, Inc.), in combination with a VERTEX 70 Fourier-transform infrared spectrometer (Bruker, Inc., Billerica, MA, USA), was used for these measurements. A silicon carbide globar was the infrared light source. The 15× Cassegrain objective, with a square 20 µm × 20 µm aperture provided an average angle of incidence $\theta$ of 8.7° on the photonic crystal structure in air with an angular spread of 0.6°. A schematic of the testing apparatus is given in Figure 3.8. All reflection measurements were taken at room temperature. A bulk gold sample was used to normalize all reflection measurements.

### 3.2.3 Results and Discussion

Experimental Fourier-transform reflection measurements (dashed black) taken during compressive testing and best-model calculated data (solid red) were plotted, and shown in Figure 3.9. The measurements were taken with the window in place. For

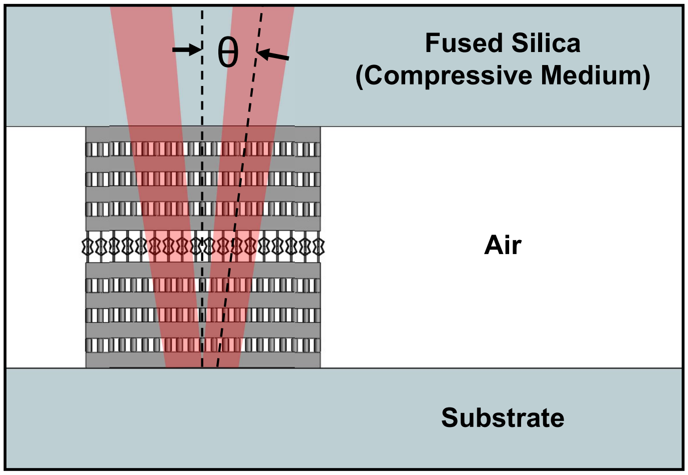

Figure 3.8: Cross-sectional schematic of the one-dimensional photonic crystal during compressive testing. The compressive medium (fused silica) is shown in contact with the photonic crystal structure. The photonic crystal is illuminated by a Cassegrain objective. For the 20 µm × 20 µm square aperture setting the average angle of incidence $\theta$ on the sample was 8.7° (in air) with an angular spread of 0.6°, shown here as the red beam path regions. This illumination was radially symmetric with respect to the normal axis.

the measurements shown in Figure 3.9 (a), Kapton tape with a thickness greater than the height of the photonic crystals was placed on the edges of the window to act as a spacer and to prevent compression. In Figure 3.9 (b), reflection measurements were taken without this Kapton tape, allowing the window to come in contact with the photonic crystals and compress the structures. Both (a) and (b) show a photonic bandgap centered at 2535 $\text{cm}^{-1}$. As a 0.84 mN compression was applied to the photonic crystal, defect resonance shifted into the photonic bandgap. Here, a very good agreement could be seen between the experimental data and the best-fit stratified-layer optical model.

The stratified-layer optical model of the design was used to perform the best-fit analysis of the experimental data. The dielectric functions of IP-Dip, the compressive medium and substrate (fused silica) were previously determined using spectroscopic ellipsometry and were not varied in this model [28, 55]. A fit analysis was performed by varying geometric model parameters, including the following: high- and low-density

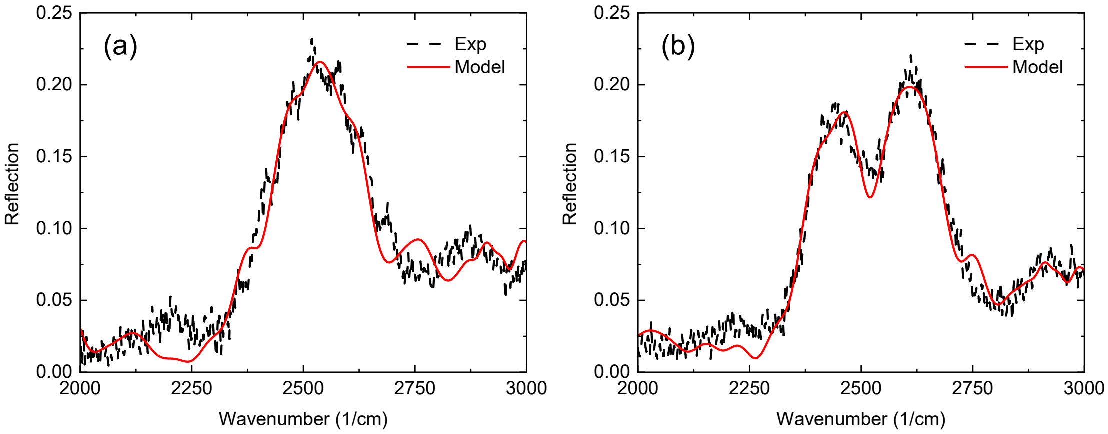

Figure 3.9: Experimental reflection measurements (black dashed lines) taken before (a) and during (b) compression of the photonic crystal and best-fit models (red solid lines). Measurements were taken through the fused silica window. The feature dominating the spectra was the photonic bandgap, which was centered around 2535 $\text{cm}^{-1}$. During compression, a transmissive defect resonance was observed within the photonic bandgap. The experimental and best-model calculated reflection data were in good agreement.

layer thicknesses, defect layer thickness, and the volumetric fill factors for both the low-density and defect layers. A Levenberg–Marquardt-based algorithm was used to vary the model parameters until a best-fit was reached between the calculated and the experimental reflection data.

The best-fit model layer thicknesses for the uncompressed photonic crystal (Figure 3.9 (a)) were determined to be (3.165 ± 0.015) µm for the high-density layer, (2.937 ± 0.026) µm for the low-density layer, and (6.7 ± 0.1) µm for the defect layer. The best-fit volumetric fill factor for the defect layer was determined to be $f_i = 0.02 \pm 0.02$. The best-fit model layer thicknesses for the compressed photonic crystal (Figure 3.9 (b)) were determined to be (3.202 ± 0.033) µm for the high-density layer, (2.844 ± 0.025) µm for the low-density layer, and (4.1 ± 0.1) µm for the defect layer. The best-fit volumetric fill factor for the defect layer was determined to be $f_i = 0.33 \pm 0.08$. During the best-model analyses the overall layer thickness non-uniformity and the low-density volumetric fill factor was assumed to be consistent between uncompressed and compressed states. The calculated layer thickness non-uniformity and low-density volumetric fill factor were found to be 4.4 ± 0.7 and $f_i = 0.41 \pm 0.02$, respectively.

During compression, the defect layer thickness was calculated and shown to have reduced to (4.1 ± 0.1) µm from (6.7 ± 0.1) µm. Based on this layer displacement, the defect layer, as an array, showed a stiffness of 315 µN/µm to the applied 0.84 mN compression. Since the defect layer consisted of an 18 × 18 array of bow-tie flexures, this suggested the spring constant of a single flexure was roughly 0.97 µN/µm following Hooke's Law.

To verify elasticity in the defect layer, reflection measurements were taken before and after the compression of the photonic crystal structure. These measurements are given in Figure 3.10. For this comparison, measurements were taken without the presence of the window. The lack of compressive loading resulted in an increase in

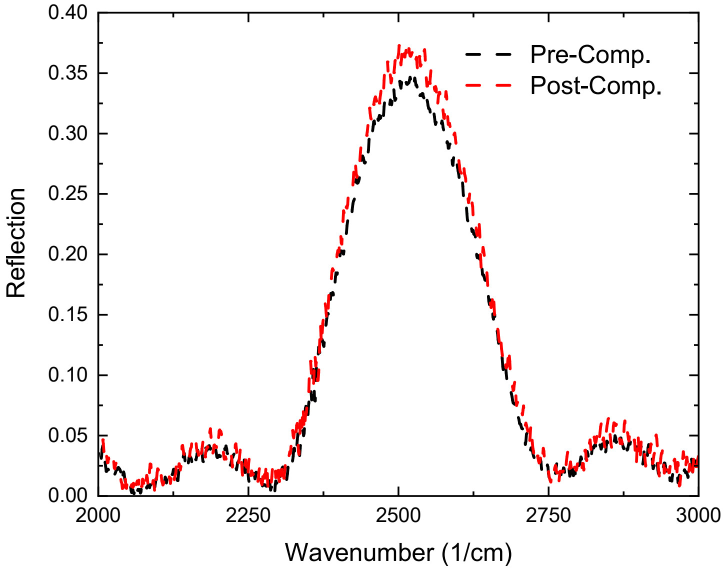

Figure 3.10: Experimental reflection measurements of the photonic crystals before (black) and after (red) compressive testing. Both measurements were taken in air, without the presence of the fused silica window. A slight amplitude change was observed as a result of the compressive testing. No other spectral changes to the photonic bandgap were distinguishable.

bandgap amplitude when compared with the measurements in Figure 3.9. The black curve in Figure 3.10 reflects the situation before any compressive contact was made with the photonic crystal structure. The reflection spectra given by the red curve refer to the situation after the compressive load was removed from the photonic crystal structure. The defect-mode resonance which was present during contact (Figure 3.9b) was no longer located within the photonic bandgap. It can be seen that the amplitude, broadening, and spectral center of the photonic bandgap were very near to those measured before compression (black).

### 3.2.4 Conclusions

A one-dimensional photonic crystal with a mechanical defect layer was fabricated by two-photon polymerization. Under compression, a defect resonance was induced within the observed photonic bandgap. Best-fit analyses of the measured reflection spectra were performed using a simple stratified-layer optical model. Very good agreement between the measured and optical model calculations was observed. The best-fit calculated layer thicknesses were found to be within ±6% when compared with the nominal layer thicknesses. Confidence intervals for the calculated layer thicknesses were comparable to a previous publication, where modeled layer thicknesses were verified by scanning electron microscope imaging [17]. The best-modeled volumetric fill factor for the low-density layers was calculated to be higher than the nominal fill factor. This indicated that the pillar diameters were wider than designed, resulting in the overall larger volume of inclusion material (IP-Dip) within these layers. This may have been a result of swelling effects, which are known to occur during the sample rinsing process [17].

The change in thickness of the defect layer as a result of compression was calculated. This displacement was used to estimate the stiffness of the bow-tie flexures used in the defect layer array. The spring constant of a single bow-tie flexure was calculated to be 0.97 µN/µm. When compared with previously reported microsprings of similar geometric scale fabricated by two-photon polymerization, this spring constant was found to be in the same order of magnitude [56]. It was also observed that the volume fill factor for the defect layer increased during compression. This aligns with expected compression effects. As the layer thickness decreases there is a larger inclusion (IP-Dip) to host medium (air) ratio within this layer.

To verify the elasticity of the defect layer, reflection measurements were taken before and after compressive testing. These measurements verified that the photonic bandgap returns to its original spectral response once compressive force is removed. Changes to the bandgap were unremarkable. These measurements suggest that, after removing the compressive force, the defect layer expands, allowing for the defect resonance to return to its original location, outside the photonic bandgap. Based on this relaxation of the defect layer, composed of a flexible bow-tie array, we suspect this degree of compressive force did not cause appreciable plastic deformation in the photonic crystal.

The observed spectral response, as a result of changes in defect layer thickness, aligned with that of our previous terahertz study [50]. In contrast to the terahertz study, where the defect layer was designed to be an air gap, the defect layer here was attached to the photonic crystal, thus fixing the initial thickness as a result of the bow-tie array geometry. When comparing the degree of defect resonance shifting between these studies, the degree of compression necessary to induce a centralized defect resonance reduced by roughly 50%. Thus, the photonic crystal presented in this study demonstrates a higher sensitivity to changes in layer thickness than what has been previously reported.

The presented results demonstrate the first successful fabrication of a one-dimensional photonic crystal with a mechanically tunable defect, fabricated by means of two-photon polymerization. As designed, the presence of a defect resonance was controlled by applying a compressive force to the photonic crystal structure. Very good agreement was found between the experimental and model calculated data. Using the defect layer thicknesses obtained from performing best-model analyses of the experimental spectra, the mechanical properties of the defect layer were estimated. The calculated mechanical properties of a single flexure agreed with spring constants reported previously for microsprings fabricated by two-photon polymerization from the same material (IP-Dip) on this same geometric scale [56]. Based on the findings of this study, we feel the designed one-dimensional photonic crystal can function as a sensitive mechanical sensor. Such functionality is desired in applications, such as microrobotics, and in MOEMS systems [35].

# REFERENCES

[1] M. Steel, M. Levy, and R. Osgood, "High transmission enhanced Faraday rotation in one-dimensional photonic crystals with defects," *J. IEEE Photonic Tech. L.* **12**, 1171 (2000).

[2] H. Jiang, H. Chen, H. Li, Y. Zhang, and S. Zhu, "Omnidirectional gap and defect mode of one-dimensional photonic crystals containing negative-index materials," *Appl. Phys. Lett.* **83**, 5386 (2003).

[3] B.-F. Wan, Z.-W. Zhou, Y. Xu, and H.-F. Zhang, "A theoretical proposal for a refractive index and angle sensor based on one-dimensional photonic crystals," *IEEE Sensors Journal* **21**, 331 (2020).

[4] R. Nelson and J. Haus, "One-dimensional photonic crystals in reflection geometry for optical applications," *Appl. Phys. Lett.* **83**, 1089 (2003).

[5] A. H. Aly, H. A. Elsayed, and C. Malek, "Defect modes properties in one-dimensional photonic crystals employing a superconducting nanocomposite material," *Opt. Appl.* **48**, 53 (2018).

[6] J. Xia, Q. Qiao, G. Zhou, F. S. Chau, and G. Zhou, "Opto-mechanical photonic crystal cavities for sensing application," *Appl. Sci.* **10**, 7080 (2020).

[7] S. Park, Y. Li, B. Norton, M. McLamb, G. D. Boreman, and T. Hofmann, "One-dimensional Photonic Crystals Fabricated Using Stereolithographic Single Layer Assembly for the Terahertz Spectral Rangee," *J. Infrared Millim. Te.* **41**, 542 (2020).

[8] C.-J. Wu and Z.-H. Wang, "Properties of defect modes in one-dimensional photonic crystals," *Pr. Electromagn. Res.* **103**, 169 (2010).

[9] E. Yablonovitch, "Photonic crystals," *J. Mod. Optic.* **41**, 173 (1994).

[10] S. John, “Strong localization of photons in certain disordered dielectric superlattices,” *Phys. Rev. Lett.* **58**, 2486 (1987).

[11] Y. Li, D. Fullager, S. Park, D. Childers, R. Fesperman, G. Boreman, and T. Hofmann, “High-contrast infrared polymer photonic crystals fabricated by direct laser writing,” *Opt. Lett.* **43**, 4711 (2018).

[12] A. Sánchez, A. V. Porta, and S. Orozco, “Photonic band-gap and defect modes of a one-dimensional photonic crystal under localized compression,” *J. Appl. Phys.* **121**, 173101 (2017).

[13] H. Shen, Z. Wang, Y. Wu, and B. Yang, “One-dimensional photonic crystals: fabrication, responsiveness and emerging applications in 3D construction,” *RSC Adv.* **6**, 4505 (2016).

[14] R. Langer, A. Barski, J. Simon, N. Pelekanos, O. Konovalov, R. Andre, and L. S. Dang, “High-reflectivity GaN/GaAlN Bragg mirrors at blue/green wavelengths grown by molecular beam epitaxy,” *Appl. Phys. Lett.* **74**, 3610 (1999).

[15] M. V. Rybin, I. I. Shishkin, K. B. Samusev, P. A. Belov, Y. S. Kivshar, R. V. Kiyan, *et al.*, “Band structure of photonic crystals fabricated by two-photon polymerization,” *Crystals* **5**, 61 (2015).

[16] R. Houbertz, P. Declerck, S. Passinger, A. Ovsianikov, J. Serbin, and B. Chichkov, “Investigations on the generation of photonic crystals using two-photon polymerization (2PP) of inorganic–organic hybrid polymers with ultra-short laser pulses,” *Phys. Status Solidi A.* **204**, 3662 (2007).

[17] V. P. Stinson, S. Park, M. McLamb, G. Boreman, and T. Hofmann, “Photonic Crystals with a Defect Fabricated by Two-Photon Polymerization for the Infrared Spectral Range,” *Optics* **2**, 284 (2021).

[18] K.-S. Lee, D.-Y. Yang, S. H. Park, and R. H. Kim, "Recent developments in the use of two-photon polymerization in precise 2d and 3d microfabrications," *Polym. Advan. Technol.* **17**, 72 (2006).

[19] Y. Lin and J. Xu, "Microstructures Fabricated by Two-Photon Polymerization and Their Remote Manipulation Techniques: Toward 3D Printing of Micromachines," *Adv. Opt. Mater.* **6**, 1701359 (2018).

[20] S. Juodkazis, V. Mizeikis, K. K. Seet, H. Misawa, and U. G. Wegst, "Mechanical properties and tuning of three-dimensional polymeric photonic crystals," *Appl. Phys. Lett.* **91**, 241904 (2007).

[21] R. Zhang, Q. Wang, and X. Zheng, "Flexible mechanochromic photonic crystals: routes to visual sensors and their mechanical properties," *J. Mater. Chem. C* **6**, 3182 (2018).

[22] C. Jansen, S. Wietzke, V. Astley, D. M. Mittleman, and M. Koch, "Mechanically flexible polymeric compound one-dimensional photonic crystals for terahertz frequencies," *Appl. Phys. Lett.* **96**, 111108 (2010).

[23] S. Park, B. Norton, G. D. Boreman, and T. Hofmann, "Mechanical tuning of the terahertz photonic bandgap of 3D-printed one-dimensional photonic crystals," *J. Infrared Millim. Te.* **42**, 220 (2021).

[24] R. K. Jayne, T. J. Stark, J. B. Reeves, D. J. Bishop, and A. E. White, "Dynamic Actuation of Soft 3D Micromechanical Structures Using Micro-Electromechanical Systems (MEMS)," *Adv. Mater. Technol.* **3**, 1700293 (2018).

[25] A. E. H. Love, *Treatise on the Mathematical Theory of Elasticity*, Cambridge University Press, (1892).

[26] J. Bauer, A. Guell Izard, Y. Zhang, T. Baldacchini, and L. Valdevit, "Programmable mechanical properties of two-photon polymerized materials: from nanowires to bulk," *Adv. Mater. Technol.* **4**, 1900146 (2019).

[27] I. S. Ladner, M. A. Cullinan, and S. K. Saha, "Tensile properties of polymer nanowires fabricated via two-photon lithography," *RSC Adv.* **9**, 28808 (2019).

[28] D. B. Fullager, G. D. Boreman, and T. Hofmann, "Infrared dielectric response of nanoscribe IP-dip and IP-L monomers after polymerization from 250 $\mathrm{cm}^{-1}$ to 6000 $\mathrm{cm}^{-1}$," *Opt. Mater. Express* **7**, 888 (2017).

[29] W. Cai and V. M. Shalaev, *Optical metamaterials*, vol. 10, Springer, (2010).

[30] S. Park, Y. Li, M. McLamb, B. Norton, G. D. Boreman, and T. Hofmann, "Highly Localized Defect Mode in Polymer-Based THz Photonic Crystals Fabricated Using Stereolithography," *J. Infrared Millim. Te.* **41**, 825 (2020).

[31] J.-F. Xing, M.-L. Zheng, and X.-M. Duan, "Two-photon polymerization microfabrication of hydrogels: an advanced 3D printing technology for tissue engineering and drug delivery," *Chem. Soc. Rev.* **44**, 5031 (2015).

[32] D. Tan, Y. Li, F. Qi, H. Yang, Q. Gong, X. Dong, and X. Duan, "Reduction in feature size of two-photon polymerization using SCR500," *Appl. Phys. Lett.* **90**, 071106 (2007).

[33] Y.-L. Zhang, Q.-D. Chen, H. Xia, and H.-B. Sun, "Designable 3D nanofabrication by femtosecond laser direct writing," *Nano Today* **5**, 435 (2010).

[34] K. S. Worthington, L. A. Wiley, E. E. Kaalberg, M. M. Collins, R. F. Mullins, E. M. Stone, and B. A. Tucker, "Two-photon polymerization for production of human iPSC-derived retinal cell grafts," *Acta Biomater.* **55**, 385 (2017).

[35] Z. Lao, N. Xia, S. Wang, T. Xu, X. Wu, and L. Zhang, "Tethered and Untethered 3D Microactuators Fabricated by Two-Photon Polymerization: A Review," *Micromachines* **12**, 465 (2021).

[36] Y. Yue and J. P. Gong, "Tunable one-dimensional photonic crystals from soft materials," *J. Photoch. Photobio. C* **23**, 45 (2015).

[37] V. A. Tolmachev, A. V. Baldycheva, K. Berwick, and T. S. Perova, "Influence of fluctuations of the geometrical parameters on the photonic band gaps in one-dimensional photonic crystals," *Pr. Electromagn. Res.* **126**, 285 (2012).

[38] F. Scotognella, A. Chiasera, L. Criante, E. Aluicio-Sarduy, S. Varas, S. Pelli, A. Łukowiak, *et al.*, "Metal oxide one dimensional photonic crystals made by RF sputtering and spin coating," *Ceram. Int.* **41**, 8655 (2015).

[39] V. P. Stinson, N. Shuchi, M. McLamb, G. D. Boreman, and T. Hofmann, "Mechanical Control of the Optical Bandgap in One-Dimensional Photonic Crystals," *Micromachines* **13**, 2248 (2022).

[40] A. H. Aly and H. A. Elsayed, "Defect mode properties in a one-dimensional photonic crystal," *Physica B* **407**, 120 (2012).

[41] H.-Y. Lee and T. Yao, "Design and evaluation of omnidirectional one-dimensional photonic crystals," *J. Appl. Phys.* **93**, 819 (2003).

[42] A. Vinogradov, A. Dorofeenko, S. Erokhin, M. Inoue, A. Lisyansky, A. Merzlikin, and A. Granovsky, "Surface state peculiarities in one-dimensional photonic crystal interfaces," *Physical Review B* **74**, 045128 (2006).

[43] L. Ding, Y. Li, C. Zhou, M. Hu, Y. Xiong, and Z. Zeng, "In-fiber Mach-Zehnder interferometer based on three-core fiber for measurement of directional bending," *Sensors* **19**, 205 (2019).

[44] S. K. Jindal, S. K. Raghuwanshi, and A. Kumar, “Realization of MOEMS pressure sensor using mach zehnder interferometer,” *J. Mech. Sci. Technol.* **29**, 3831 (2015).

[45] S. Agarwal, J. K. Mishra, and V. Priye, “Highly sensitive MOEMS integrated photonic crystal cavity resonator for nano-mechanical sensing,” *Opt. Commun.* **474**, 126150 (2020).

[46] V. S. Chaudhary, D. Kumar, R. Mishra, and S. Sharma, “Hybrid dual core photonic crystal fiber as hydrostatic pressure sensor,” *Optik* **210**, 164497 (2020).

[47] R. Rajasekar and S. Robinson, “Nano-pressure and temperature sensor based on hexagonal photonic crystal ring resonator,” *Plasmonics* **14**, 3 (2019).

[48] L. V. Nguyen, E. P. Schartner, D. Otten, Z. Yu, D. Lancaster, H. Ebendorff-Heidepriem, and S. C. Warren-Smith, “Multi-point optical fiber pressure sensor,” *AOS Australian Conference on Optical Fibre Technology (ACOFT) and Australian Conference on Optics, Lasers, and Spectroscopy (ACOLS) 2019* **11200**, 40 (2019).

[49] A. M. Upadhyaya, M. K. Hasan, S. Abdel-Khalek, R. Hassan, M. C. Srivastava, P. Sharan, *et al.*, “A comprehensive review on the optical micro-electromechanical sensors for the biomedical application,” *Front. Public Health* **9**, 759032 (2021).

[50] S. Park, V. P. Stinson, M. McLamb, G. D. Boreman, and T. Hofmann, “Mechanical tuning of defect modes in polymer-based terahertz one-dimensional photonic crystals fabricated by stereolithography,” *Opt. Eng.* **60**, 117104 (2021).

[51] B. S. Calin and I. A. Paun, “A Review on Stimuli-Actuated 3D Micro/Nanostructures for Tissue Engineering and the Potential of Laser-Direct

Writing via Two-Photon Polymerization for Structure Fabrication," *Int. J. Mol. Sci.* **23**, 14270 (2022).

[52] I. A. Păun, C. C. Mustăciosu, R. C. Popescu, B. Ş. Călin, and M. Mihăilescu, "Collagen/chitosan functionalization of complex 3d structures fabricated by laser direct writing via two-photon polymerization for enhanced osteogenesis," *Int. J. Mol. Sci.* **21**, 6426 (2020).

[53] I. A. Paun, M. Zamfirescu, C. R. Luculescu, A. M. Acasandrei, C. C. Mustaciosu, M. Mihailescu, and M. Dinescu, "Electrically responsive microreservoires for controllable delivery of dexamethasone in bone tissue engineering," *Appl. Surf. Sci.* **392**, 321 (2017).

[54] Y. F. Joya, T. Wang, and Z. Liu, "Formation and antibacterial activities of nanostructured TiO2 based thin films by sol-gel/laser-induced technique," *International Congress on Applications of Lasers & Electro-Optics* **2011**, 1152 (2011).

[55] Y. Li, D. Fullager, E. Angelbello, D. Childers, G. Boreman, and T. Hofmann, "Broadband near-infrared antireflection coatings fabricated by three-dimensional direct laser writing," *Opt. Lett.* **43**, 239 (2018).

[56] X. Shang, N. Wang, Z. Wang, H. Jiang, Y. Jia, N. Zhou, and M. Qiu, "Customizable and highly sensitive 3d micro-springs produced by two-photon polymerizations with improved post-treatment processes," *Appl. Phys. Lett.* **120**, 171107 (2022).

# CHAPTER 4: DIFFRACTIVE OPTICS FOR MICRO-MECHANICAL APPLICATIONS

## 4.1 Towards Two-Photon Polymerization-Compatible Diffractive Optics for Micro-Mechanical Applications

Diffractive optics are structured optical surfaces that manipulate light based on the principles of interference and diffraction.[1] By carefully designing the diffractive optical elements, the amplitude, phase, direction, and polarization of the transmitted and reflected light can be controlled. It is well-known that the propagation of light through diffractive optics is sensitive to changes in their structural parameters. In this study, a numerical analysis is conducted to evaluate the capabilities of slanted-wire diffraction gratings to function opto-mechanically in the infrared spectral range. The slanted wire array is designed such that it is compatible with fabrication by two-photon polymerization, a direct laser-writing approach. The modeled optical and mechanical capabilities of the diffraction grating are presented. The numerical results demonstrate a high sensitivity of the diffracted light to changes in the slant angle of the wires. The compressive force by which desired slant angles may be achieved as a function of the number of wires in the grating is investigated. The ability to fabricate the presented design using two-photon polymerization is supported by the development of a prototype. The results of this study suggest that slanted-wire gratings fabricated using two-photon polymerization may be effective in applications such as tunable beam splitting and micro-mechanical sensing.

---

[1] Reprinted with permission from V. P. Stinson, U. Subash, M. K. Poutous, and T. Hofmann, "Towards Two-Photon Polymerization-Compatible Diffractive Optics for Micro-Mechanical Applications," *Micromachines* **14**, 1319 (2023). © 2023, MDPI.

### 4.1.1 Introduction

Diffraction gratings have a wide range of applications such as holography, spectral analysis, integrated optics, quantum electronics, etc. [1]. For applications such as spectral filtering [2, 3], antireflection [4], and waveguide coupling [5], diffractive gratings are used to optimize the system transmission efficiencies. Other applications such as pulse shaping, mode locking, Q switching, multiplexing, demultiplexing, spatial light modulation, and multiple-beam generation also depend on gratings [1]. While all these applications are distinct, they all exploit the same basic diffraction properties of a grating.

Slanted-wire gratings are an efficient design for light coupling into waveguides, which is essential in applications such as liquid crystal displays, virtual reality displays, and backlighting and has been studied for over a decade [6]. While these applications are in the visible regime, slanted gratings are also optimized for performance in the infrared regime for applications such as multi-mode interference (MMI) couplers [7]. Slanted gratings have advantages over traditional binary rectangular gratings as they can be operated at normal incidence, a useful feature in integrated optics, as it eases the complexity of alignment.

Slanted gratings are fabricated mainly using electron-beam lithography and reactive ion etching (RIE) processes. To etch at oblique angles, an equipotential Faraday cage is placed over the substrate resting at an oblique angle with the platten of the etching chamber [8]. Fabrication by focused ion beam etching using an alumina hard mask and iodine gas have also been reported [9]. Fabrication errors such as a deviation from the nominal design depth, fill factor, and distorted side walls are common in RIE-fabricated gratings due to shadowing effects [10].

While these approaches have advantages in their scalability, they require the use of sophisticated processes that can be costly and time consuming and are not applicable for rapid prototyping. The use of additive manufacturing to fabricate optics has seen attention in recent years [11]. The main advantage of 3D-printing processes is their ability to synthesize nearly arbitrary geometries. Two-photon polymerization has been the additive-manufacturing technique of choice for the development of optical devices for applications in the visible and infrared spectral range. Using this technique, resolutions can be attained below the diffraction limit of the light source [11]. This was first demonstrated in 2001 by S. Kawata et al., who successfully printed a bull figurine with feature sizes of 120 nm [12].

The ability of two-photon polymerization to fabricate nearly arbitrary geometries on a sub-wavelength scale is a powerful tool in the development of structures that manipulate light by diffraction. The applications of diffractive optics fabricated with this technique are expansive, ranging from biological applications such as fiber-optical microendoscopy [13] to wide-scope "lab on a fiber" devices for applications in chemical and temperature sensing [14].

In addition to the synthesis of optical devices, two-photon polymerization has been implemented in fabricating micro-mechanical systems [15–18]. Structures fabricated with this approach can be designed to have elastic functionality. As interest has grown in this area, studies have been conducted to characterize the mechanical properties of many two-photon polymerization-compatible resins [19–22]. These mechanical properties have been exploited to develop devices such as micro-electromechanical systems (MEMS) [16], biomaterial scaffolds [17], and magnetic micro-robots [18].

There is interest in combining optical and micro-mechanical capabilities in a single device. These devices are often termed "MOEMS," which stands for micro-optical electromechanical systems. MOEMS have a range of applications in fields such as communication technology, medicine, and aerospace [23]. The utilization of MOEMS ranges from simple micro-mirror arrays [24] and photonic switches [25] to more sophisticated applications such as micro-spectrometers [26]. However, reports on devices with opto-mechanical capabilities fabricated by two-photon polymerization are scarce [27–29].

Micro-scale slanted-wire arrays have been realized with two-photon polymerization [30, 31]. The slanted wires fabricated in these studies are on a scale that could function in the infrared spectral range as diffractive gratings. However, there has not yet been an investigation of slanted-wire diffractive gratings fabricated with this technique. The fabrication of slanted-wire gratings using two-photon polymerization could be an impactful next step in diffractive optics. While these off-axis gratings currently require a more sophisticated fabrication approach than axis-symmetric gratings, they pose no additional intricacies for fabrication with two-photon polymerization.

In this study, we numerically investigate the potential of combining the mechanical properties of a two-photon polymerization-compatible material (IP-Dip) with the unique functionality of slanted-wire diffraction gratings. Using a rigorous coupled-wave analysis approach, a slanted wire grating geometry is optimized to transfer power between the 0th and +1st order as a function of compression. The mechanical nature of the designed slanted wire grating is then investigated using finite element method simulations. The promising results of this numerical investigation suggest slanted-wire gratings fabricated with two-photon polymerization may be effective in applications such as micro-mechanical sensing and tunable beam splitting. The ability to realize the designed grating with two-photon polymerization is verified by the fabrication of a prototype. The quality of the prototype is determined using scanning electron microscope (SEM) imaging.

### 4.1.2 Model Design

General diffractive concepts can be used to explain the distinct diffractive characteristics that are frequently observed in slanted-wire gratings. The slant angle is specifically selected to be close to the first Bragg angle, to increase the first diffracted order efficiency [32]. The structure parameters of the grating were designed such that only the 0th and +1st diffracted orders will be able to propagate under normal incidence conditions. This follows directly from the diffraction equation:

$$\begin{aligned} n_\mathrm{t}\sin\theta_{\mathrm{t}m} - n_\mathrm{i}\sin\theta_\mathrm{i} &= m\left(\tfrac{\lambda}{\Lambda}\right)\sin\phi, \\ m &= 0, \pm1, \pm2, \pm3\ldots \end{aligned} \tag{4.1}$$

where $n_\mathrm{i}$ and $n_\mathrm{t}$ are the indices of refraction of the incident and transmitted directions, respectively. $\Lambda$ and $\phi$ are the period and slant angle, respectively, as seen in Figure 4.1, and $\theta_{\mathrm{t}m}$ and $\theta_\mathrm{i}$ are the diffracted angle for the $m$th order and the incident angle, respectively. As the ratio $\lambda\sin\phi/\Lambda$ approaches 1, the value of orders $m$ for which the diffracted angle is real approaches zero (Equation (4.1)), indicating that the diffracted orders become progressively evanescent. Light propagates through the grating medium only for diffracted orders resulting from real angle values. This relationship can be exploited to effectively limit the number of propagating orders to two. This can be achieved by intentionally designing the grating period $\Lambda$ such that it closely matches the operating wavelength $\lambda$.

Rigorous coupled-wave analysis was used in combination with the diffraction equation to calculate the diffraction efficiency, as well as the diffraction angles $\theta_{\mathrm{t}m}$ [1]. The investigated slant angle range was restricted from 35° to 45° in order to minimize the possible inaccuracies that may result from deformations in the wire geometry during compression.

The material that was selected to design the grating for these simulations was a two-photon polymerization-compatible resin (IP-Dip). This resin provides transparency bands in the infrared and allows nanoscale resolution using two-photon polymerization [33, 34]. The optical properties of IP-Dip that are used in this model have been previously determined using spectroscopic ellipsometry and are described in detail in Ref. 33. As a starting configuration, the geometric structure parameters were adapted from a previous investigation of slanted-wire arrays that were successfully fabricated from IP-Dip using two-photon polymerization (see Ref. 31).

The slanted wire grating is described by several structure parameters. These parameters are shown in the inset of Figure 4.1. The wire width $w$, length $L$, and periodicity $\Lambda$ were varied in order to optimize the transmitted diffraction pattern. The slant angle $\phi$ was set to 45°. The design wavelength was selected to be 4 µm. X-axis linearly polarized light at normal incidence is assumed, which follows the in-plane direction of the slanted wires, as shown in the inset of Figure 4.1. Fused silica is selected as the substrate due to its compatibility with two-photon polymerization fabrication. The dielectric properties of the substrate were determined using spectroscopic ellipsometry.

Following the selection of the grating parameters, mechanical analysis was conducted. The Structural Mechanics module of COMSOL Multiphysics was used for finite element method mechanical simulations of a single slanted wire. The slanted wire is assumed to be an isotropic linear elastic material. During computation, the mechanical deformation was calculated using a 6 × 6 elasticity matrix [35].

The mechanical properties used for IP-Dip in this model were taken from Refs. 21 and 22. The design used for mechanical simulation is given in Figure 4.2. The configuration consists of three main parts, upper and lower platforms and a single slanted wire. The platforms act as regions of attachment. The lower platform simulates the substrate on which the slanted wires are fabricated and thus, it remains fixed

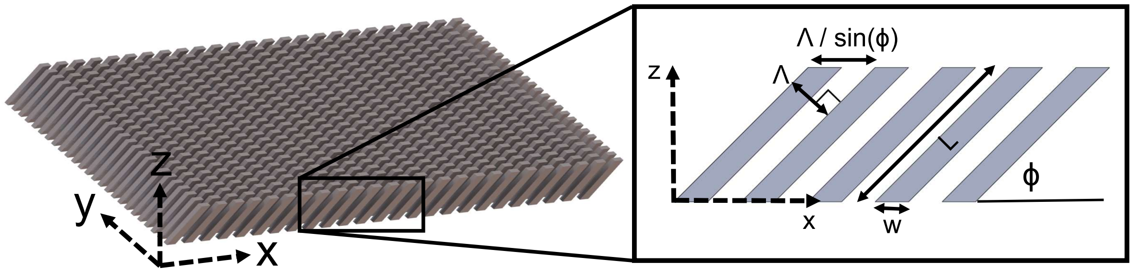

Figure 4.1: CAD model of the slanted-wire diffraction grating investigated here. During simulation, the wire width $w$, length $L$, x-axis projection of the grating period $\Lambda/\sin\phi$, and slant angle $\phi$ were varied to optimize the design.

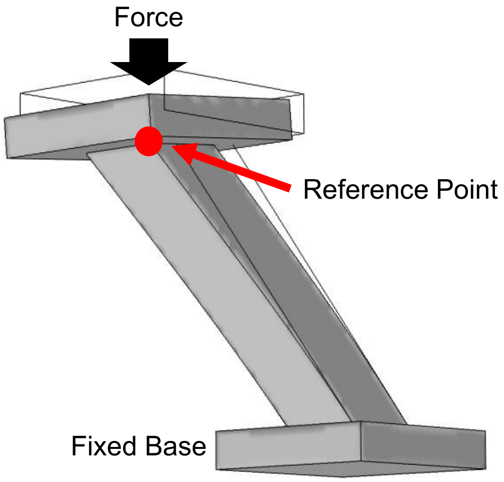

Figure 4.2: Design used for mechanical simulation in COMSOL Multiphysics. Top and bottom platforms can be seen on each end of a single slanted wire. The bottom platform is fixed while the top platform and wire are free bodies. Displacement of the slanted wire is measured with respect to a reference point on the top of the slanted wire, indicated by the red dot in the diagram.

during simulation. The upper platform acts as the object that is compressing the slanted wire. The upper platform and slanted wire are free-moving, allowing them to displace and deform during simulation. As the applied force is varied, the z-axis displacement of the reference point on the slanted wire is monitored. This reference point is indicated by the red dot in Figure 4.2.

### 4.1.3 Results and Discussion

#### 4.1.3.1 Optical Simulations

The slanted-wire-grating geometry was optimized such that the transmitted diffraction order efficiencies would vary as a function of the slant angle $\phi$. Practically, such a variation can be achieved by compression. Since compression is proportional to changes in the slant angle, the wire width $w$, length $L$, and x-axis periodicity $\Lambda/\sin\phi$ were optimized using parametric sweeps to maximize the contrast in transmission efficiency as a function of the slant angle. It is worth highlighting that the diffraction orders are insensitive to changes in the y-axis periodicity. Thus, this periodicity can be selected based on fabrication constraints.

The greatest contrast was found for the configuration $w = 2.25$ µm, $L = 10$ µm, and $\Lambda/\sin\phi = 4$ µm. The calculated transmission efficiencies and geometry can be seen in Figure 4.3. As the slant angle is varied between 35° and 45°, the transmission efficiencies of the 0th (black) and +1st (red) orders share an inverse relationship while the −1st (blue) order efficiency is effectively suppressed. As the grating is compressed, resulting in a reduction in the slant angle $\phi$, the power is coupled from the 0th order ($\theta_{\mathrm{t0}} = 0°$) to the +1st order ($\theta_{+\mathrm{t1}} = 46°$). For small variations in the slant angle between $\phi = 45°$ and $\phi = 35°$, the power transferred from the 0th to the +1st order fluctuates from a minimum of 3% at $\phi = 45°$ to a maximum of 70% at $\phi = 35°$. The power is equally shared between the 0th and +1st order at $\phi = 38.4°$. It is observed that the −1st order is suppressed for all slant angles within this range.

The diffraction angles of the 0th and ±1st orders were investigated as a function of the slant angle $\phi$. It was observed that as the slant angle was varied, the diffraction angles remained constant, as shown in Figure 4.4. In this diagram, two slant angles

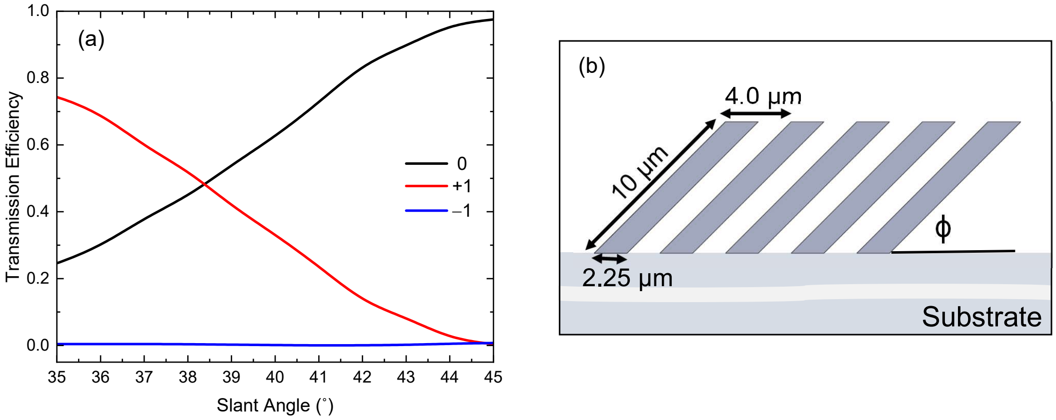

Figure 4.3: (a) Model calculations comparing the transmitted diffraction efficiencies for the 0th and ±1st orders as slant angle $\phi$ is varied. An inverse relationship is seen between the 0th (black) and +1st (red) orders while the −1st (blue) order is suppressed. (b) The optimized geometry used during this calculation. The values of the spatial parameters of the wire, $w = 2.25$ µm, $L = 10$ µm, and $\Lambda/\sin\phi = 4$ µm, are shown here.

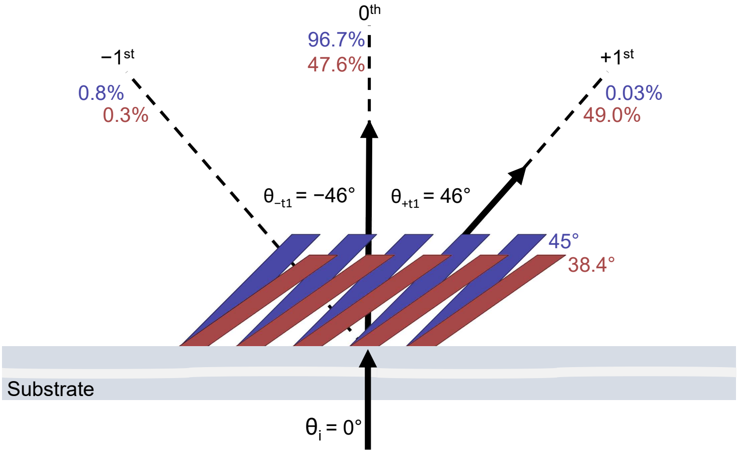

Figure 4.4: Diffraction efficiencies and diffraction angles of the 0th and ±1st orders are mapped for two slant-angle ($\phi$) geometries. The efficiencies corresponding to a slant angle are color-matched. The 45° (blue) and 38.4° (red) slant-angle geometries are exaggerated for visualization. The arrows indicate the direction of propagation of the diffracted light.

are compared. The diffraction efficiencies are provided for the different slant angles by corresponding colors. While the diffraction efficiencies vary between the 0th and +1st orders as designed, the diffraction angles do not vary.

The constant diffraction angles can be explained by investigating how compression changes the grating vector $\vec{\kappa}$, which results from the orientation of the grating lines in space and the spatial period, as shown in Figure 4.5. The direction of $\kappa$ is perpendicular to the slant of the grating. Its magnitude is inversely proportional to $\Lambda$ ($|\vec{\kappa}| = 2\pi/\Lambda$). In Figure 4.5, the grating before and after compression is shown for two different slant angles $\phi_1$ and $\phi_2$ with corresponding grating vectors $\kappa_1$ and $\kappa_2$. The angle made by $\vec{\kappa}$ with the z-axis is equal to the slant angle. The x-component of $\vec{\kappa}$, which is denoted by $\kappa_x = 2\pi \sin\phi/\Lambda$, remains constant with compression, whereas the z-component $\kappa_z$ varies. Since the ratio $\sin\phi/\Lambda$ that appears in the diffraction Equation (4.1) is a constant, the diffracted angles of the 0th and 1st diffracted orders in transmission are independent of the slant angle.

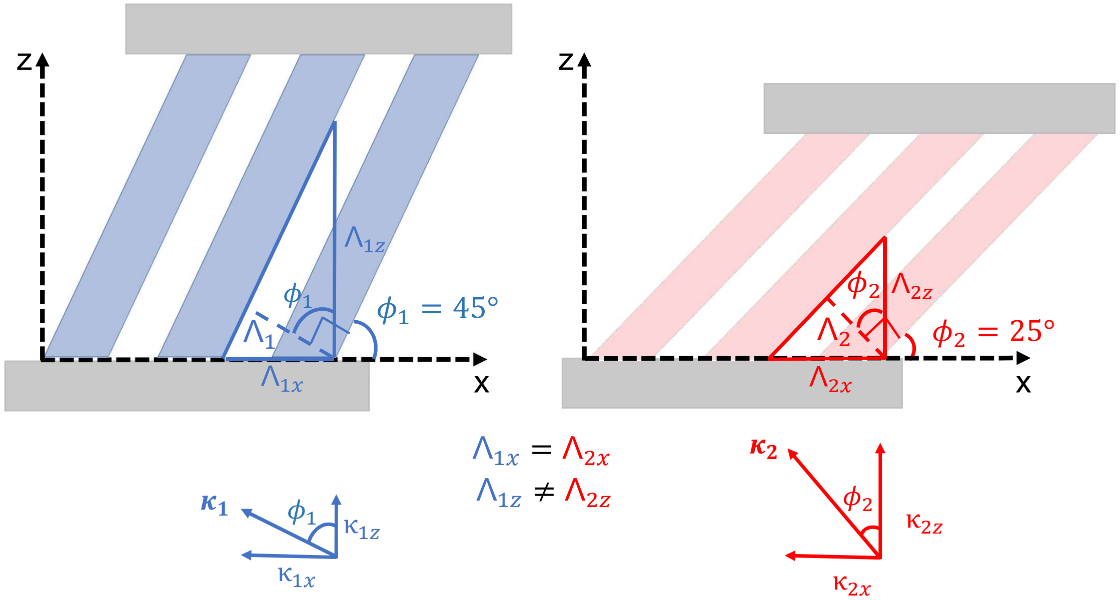

Figure 4.5: Comparison of the grating vector for two different slant angles $\phi_1$ and $\phi_2$ and their corresponding grating vector $\vec{\kappa}$. Here, the x- and z-components for $\vec{\kappa}$ and $\Lambda$ are shown. While the z-components of $\vec{\kappa}$ and $\Lambda$ vary for $\phi_1$ and $\phi_2$, the x-components remain constant.

#### 4.1.3.2 Mechanical Simulations

Finite element method simulations were conducted to characterize the mechanical capabilities of a single slanted wire. The geometry used for simulation is given in Figure 4.3 (b). The structure is defined as an isotropic linear elastic material. The mechanical properties of IP-Dip that were used during simulation were obtained from Refs. 21 and 22. These mechanical parameters included Young's modulus, Poisson's ratio, and density and were estimated to be 2.5 GPa, 0.35, and 1200 kg/m$^3$, respectively.

Figure 4.6 shows the results of finite element method simulations where a base and top platform are placed on a single slanted wire to act as attachment interfaces, as shown in Figure 4.2. The bottom surface remains fixed during simulation. A force is applied perpendicular to the top platform. The change in position of a single point is tracked as the force is varied. This reference point is shown in Figure 4.2. The results of the simulation are plotted in Figure 4.6. Here, the height change experienced by the reference point as a function of the applied force is given by the black curve. Using the calculated height change, the resulting slant angle is calculated. The slant angle as a function of the applied force is given by the red curve in Figure 4.6.

Based on the results of the mechanical simulation, the spring constant of a single wire is $k_{\mathrm{sw}} = 9.62\ \mu\mathrm{N}/\mu\mathrm{m}$. This value is calculated from the black curve in Figure 4.6 by taking the inverse of the slope, thereby obtaining the relationship between the applied force and displacement. To predict the stiffness of an entire array of slanted wires, the array can be treated as individual springs that are in parallel. In parallel, each spring shares the applied force. Applying Hooke's law, the effective spring constant $k_{\mathrm{eff}}$ is then:

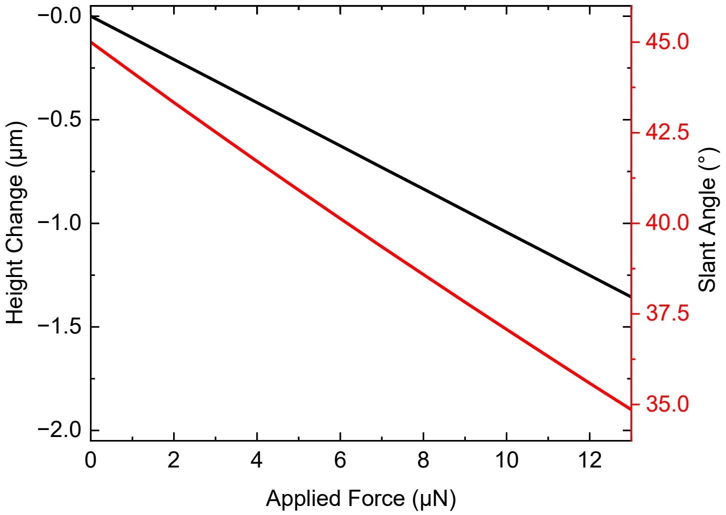

Figure 4.6: Finite element method simulated data showing the effects of applied force on the geometry of a single slanted wire are shown. The height change (black line) tracks the z-axis movement of a reference point on a single slanted wire, as shown in Figure 4.2. The effects on the slant angle (red line) as a function of applied force, calculated from the height change, are plotted on a second y-axis.

$$k_{\text{eff}} \;=\; pk_{sw}, \tag{4.2}$$

where $p$ is the number of slanted wires in an array. Using the effective spring constant for a given array size, the degree of compression experienced by the array as a function of the applied force can be calculated using Hooke's Law [36]:

$$F \;=\; k_{\text{eff}}a, \tag{4.3}$$

where $a$ is the displacement of the slanted wire in the z-direction. The force necessary to reach a desired slant angle for an array of slanted wires can be approximated by:

$$F(\phi) \;=\; k_{\text{eff}}L[\sin(\phi_{\circ}) - \sin(\phi)], \tag{4.4}$$

where $L$ is the length of a single wire, $\phi_{\circ}$ is the fabricated slant angle, and $\phi$ is the slant angle desired. $k_{\text{eff}}$ increases linearly with $p$ (Equation (4.2)); thus, a linear relationship can be expected between $p$ and the applied force needed to achieve a desired slant angle.

An analysis of this effect using the geometry given in Figure 4.3 (b) is shown in Figure 4.7. Here, the force range over which the slanted wires will function such that the slant angle $\phi$ is varied between 45° (black) and 35° (blue) is plotted with respect to the array size $p$. The grey-lined region indicates the force needed to vary the slant angle between 45° and 35° as a function of $p$. The range is limited by the force required to induce a compression resulting in a slant angle of 35° (blue).

#### 4.1.3.3 Fabrication Using Two-Photon Polymerization

A prototype of the designed slanted-wire grating was fabricated using two-photon polymerization. A geometry was selected such that the wire width and periodicity would be near that of the grating, as shown in Figure 4.3 (b). A commercial two-photon polymerization system (Photonic Professional GT, Nanoscribe, GmbH,

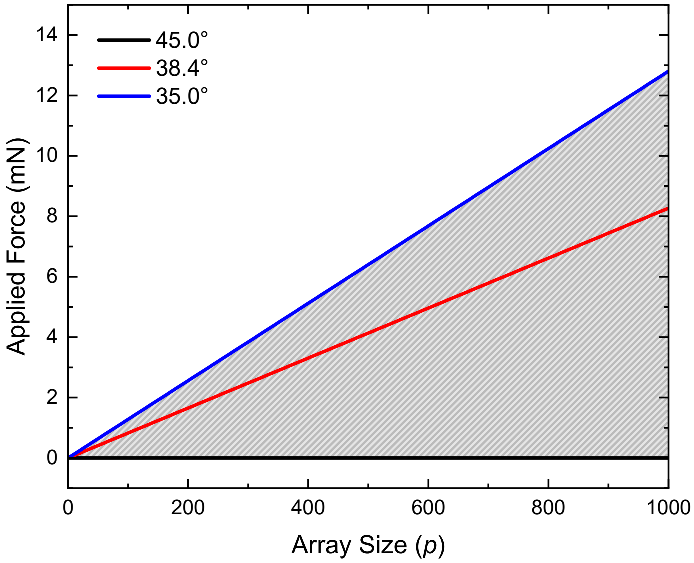

Figure 4.7: Effect of increasing array size $p$ on the applied force necessary to achieve different wire slant angles. Three slant angles are plotted: 45° (black), 38.4° (red), and 35° (blue). The grey-lined region indicates the force range over which the slanted wire array can function as designed.

Karlsruhe, Germany) was used to polymerize the design from the photosensitive resin IP-Dip. A 63× objective was used to write the structures. The best print settings were determined to be at 40% laser power (maximum 25 kW) with a 500 mm/s scan speed. The slicing and hatching distances, used to define the space between consecutive scans, were both set to 0.2 µm.

An SEM micrograph of the resulting structure is given in Figure 4.8. Here, a 10 × 10 array of slanted wires can be seen with wire dimensions and lattice periodicity near that of the nominal design provided in Figure 4.3 (b). The quality of the wire structures appears to be uniform across the array, which fills a 36 × 36 µm$^2$ area.

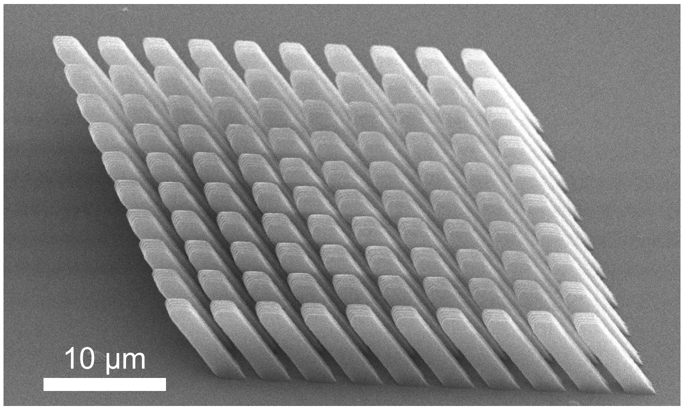

Figure 4.8: SEM micrograph of a prototype slanted-wire diffraction grating with dimensions matching the design in Figure 4.3 (b). The wires are arranged in a square lattice pattern. The wires are fabricated with high fidelity, demonstrating that mechanically modulatable three-dimensional grating structures can be obtained using two-photon polymerization.

### 4.1.4 Conclusions

A numerical investigation of slanted-wire gratings compatible with fabrication by two-photon polymerization was conducted. The optical and mechanical characteristics of the designed grating were evaluated. The grating material used to conduct this analysis was a two-photon polymerization-compatible resin IP-Dip. Using previously reported optical and mechanical properties for this resin, the grating geometry was optimized parametrically to maximize the sensitivity to changes in the slant angle. A slanted-wire grating prototype was fabricated with two-photon polymerization using the optimized grating geometry.

As the grating slant angle $\phi$ is changed under compression between 45° and 35°, the power transitions from the 0th order to the +1st order. It is observed that the $-1$st order is suppressed for all slant angles within this range. The maximum power transfer is observed at $\phi = 35°$, while the power is almost equally shared at $\phi = 38.4°$. The diffraction angles of the propagating orders are found to be constant as the slant angle is adjusted. The diffraction efficiency's sensitivity to small changes in the slant angle, while maintaining the direction of propagation, could be valuable for applications such as tunable beam splitting.

In order to evaluate the compressive functionality of the designed grating, the mechanical properties of a single wire were considered. The initial slant angle for the wire was designed to be 45°. Force was applied to the top-most surface of the wire along the z-axis to simulate the grating under compression. The change in height was monitored as a function of the applied force. This displacement was in turn used to calculate the slant angle as a function of the applied force. The spring constant of a single wire was calculated to be 9.62 µm/µN and is comparable to experimentally realized values [37].

Applying Hooke's law to springs in parallel, the force range over which the slanted wire grating can expect to operate as a function of the array size was determined. The force required to attain a slant angle of 35° increases at a rate of 12.8 µN/wire. Increasing the array size effectively decreases the grating's sensitivity to the applied force, which can be exploited to optimize the grating's functionality over a desired compressive force range. By monitoring fluctuations in either of the propagating diffractive orders, the degree of compression can be determined. These results suggest that the grating may be appropriate for applications in micro-mechanical sensing. An advantage of this sensor would be in the ability to detect mechanical changes without needing physical access to the grating.

To verify the ability to fabricate the slanted-wire grating described in this study using two-photon polymerization, a prototype was developed. The geometry for this prototype was selected to match the optimized geometry presented. The quality of the fabricated array was determined using scanning electron microscopy. It is observed that the fabricated array geometry is near that of the nominal design. The quality of the slanted wires appears to be uniform across the array.

In summary, a numerical study of slanted-wire diffraction gratings compatible with two-photon polymerization was conducted. It is observed that the propagating diffraction orders of the designed grating are extremely sensitive to small changes in the slant angle. This feature, coupled with the mechanical properties the two-photon polymerization-compatible material IP-Dip, supports the use of such a grating in applications such as tunable beam splitting and micro-mechanical sensing. By varying the constituent geometry and array size, the grating can be optimized to function over a range of wavelengths and compressive forces.

## 4.2 Slanted Wire Diffraction Gratings Fabricated by Two-Photon Polymerization

Slanted wire diffraction gratings are difficult to fabricate using conventional etching approaches, due to their off-axis symmetry.[2] In this study, we present the first fabrication of slanted wire diffraction gratings by two-photon polymerization and verify the diffractive characteristics.

### 4.2.1 Introduction

Diffractive gratings are used in many modern technologies such as holography, spectral analysis, integrated optics, and quantum electronics [1]. Slanted-wire gratings are particularly effective in waveguide coupling applications [6]. In contrast to rectangular binary gratings, slanted wire gratings can populate higher diffractive orders asymmetrically at normal incidence, a useful feature in integrated optics.

Traditionally, slanted wire gratings have been mainly fabricated by electron-beam lithography and reactive ion etching. To achieve the necessary off-axis symmetry, the substrate must be etched at oblique angles, making its fabrication more challenging than axis-symmetric gratings [8]. In this study, we expand upon a recent numerical investigation which considered the opto-mechanical potential of slanted wire diffraction gratings fabricated by two-photon polymerization [38]. As an additive manufacturing technique, the off-axis symmetry of these gratings pose no additional intricacies when fabricated by this approach.

Using a rigorous-coupled wave approach (RCWA), a slanted wire grating geometry was optimized for operation at 633 nm. Using this design, the grating was fabricated using two-photon polymerization and it's diffractive characteristics were determined. While deviations were observed from the nominal design, likely due to fabrication errors, the asymmetric population of higher diffraction orders is observed and found

---

[2] Reprinted with permission from V. P. Stinson, U. Subash, N. Shuchi, M. K. Poutous, and T. Hofmann, "Slanted Wire Diffraction Gratings Fabricated by Two-Photon Polymerization," accepted for *CLEO: Science and Innovations*, (2024). Ⓒ 2024, Optica Publishing Group.

to be in good agreement with RCWA calculation results, thus confirming the off-axis wire alignment. The results of this study demonstrate the fabrication of slanted wire diffraction gratings by two-photon polymerization for the first time.

### 4.2.2 Modeling, Fabrication, and Characterization

The optical response of the slanted wire diffraction grating was modeled using a rigorous coupled wave approach in combination with the diffraction equation. The dielectric properties of IP-Dip, a two-photon compatible resin, were determined previously using spectroscopic ellipsometry [39]. Fused Silica was selected as the substrate. Using parametric sweeping, the geometry of the slanted wire array, including wire width, wire length, slant angle, and grating period were varied. To demonstrate asymmetric population of diffraction orders at normal incidence, the grating was optimized to populate the $0^{\text{th}}$ and $+1^{\text{st}}$ orders while suppressing the $-1^{\text{st}}$ order. The optimized geometry for operation at 633 nm using x-polarized light can be seen in Fig. 4.9 (c) and the resulting diffraction pattern is given by the solid black curve in Fig. 4.9 (b).

The array was fabricated by two-photon polymerization using the Nanoscribe Photonic Professional GT system. The 63x objective was selected, the scan speed was set to 10,000 mm/s and laser power to 60% (maximum 25 kW). A 110 µm x 125 µm patch was patterned in order to create a roughly 2 mm x 2 mm array area. Microscope images taken at 10x (inset) and 100x of the fabricated array are shown in Fig. 4.9 (a). At 10x magnification, a checkered pattern can be seen as a result of stitching between the 110 µm x 125 µm patches.

The diffractive characteristics of the fabricated sample were tested using a linearly polarized 633 nm source. A Thorlabs Standard Photodiode Power Sensor, mounted on a rotation stage, was used to measure the diffraction efficiencies at various angles. The deviation from the nominal geometric design was determined using a parametric optimization, which implements a downhill simplex, in order to find agreement with

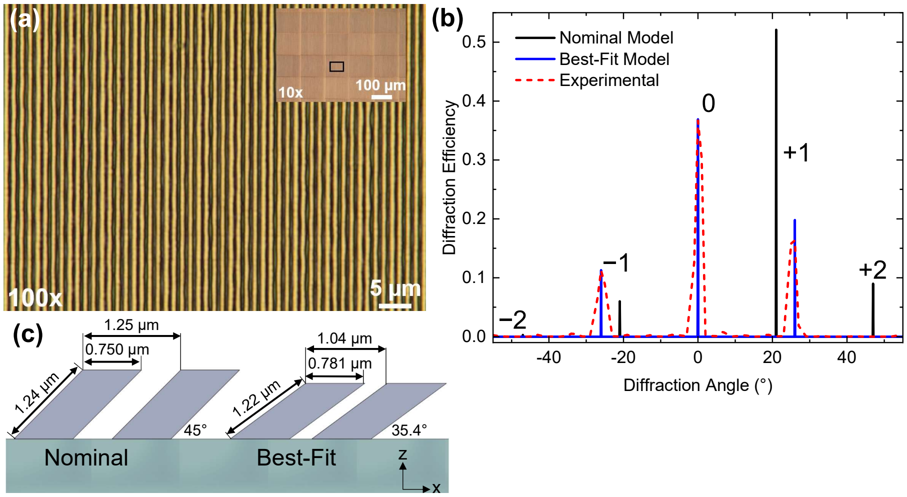

Figure 4.9: (a) Microscope images taken of a portion of the fabricated slanted wire array at 10x (inset) and 100x magnification. In the 10x image, a checkered pattern can be seen due to the stitching error introduced between adjacent sections, resulting from movement of the motor stage during the writing process. (b) Experimental (red dashed line) and model calculated (blue and black solid line) diffraction efficiency as a function of diffraction angle. (c) Comparison of the nominal and the best-fit geometries of the slanted wire array.

the experimentally observed diffraction characteristics.

### 4.2.3 Results

The experimentally measured diffraction efficiencies for the $0^{\text{th}}$ and $\pm 1^{\text{st}}$ orders are given by the red dashed curve in Fig. 4.9 (b). The efficiencies of the $-1^{\text{st}}$, $0^{\text{th}}$, and $+1^{\text{st}}$ orders were found to be 11.2±0.3%, 36.7±1.1%, and 16.3±0.5%, respectively. The diffraction angles of the $-1^{\text{st}}$ and $+1^{\text{st}}$ orders were $-26°$ and 26°, respectively. In the nominal design (see Fig. 4.9 (c)), the expected efficiencies of the $-1^{\text{st}}$, $0^{\text{th}}$, and $+1^{\text{st}}$ orders were 6.0%, 30.0%, and 52.1%, respectively. The diffraction angles of the $-1^{\text{st}}$ and $+1^{\text{st}}$ orders were $-20°$ and 20°, respectively.

The best-fit geometry, determined by parametric optimization, is given in Fig. 4.9 (c). Based on this geometry, the efficiencies of the $-1^{\text{st}}$, $0^{\text{th}}$, and $+1^{\text{st}}$ orders were calculated to be 11.3%, 36.9%, and 19.8%, respectively. The diffraction angles of the $-1^{\text{st}}$ and $+1^{\text{st}}$ orders were $-26°$ and 26°, respectively. Good agreement can be seen between the experimental (red-dashed) and best-fit model (blue solid) data given in Fig. 4.9 (b).

### 4.2.4 Conclusions

In this study, slanted wire diffraction gratings fabricated by two-photon polymerization were realized for the first time. Likely as a result of fabrication errors, the geometry of the investigated sample deviated from the nominal design. From the experimental results we conclude that the fabricated grating has possible excursions in periodicity ($-16.8\%$), duty cycle ($+25.2\%$) and phase height ($-19.4\%$). As a next step, to achieve dimensions closer to nominal, the fabrication parameters can be altered to compensate for the observed distortions (see Ref. 40).

Due to the sensitivity of gratings to changes in geometry, this deviation affected the diffractive characteristics. While the difference in efficiency between the $-1^{\text{st}}$ and $+1^{\text{st}}$ orders in the fabricated sample (9.4%) was less than the nominal model (46.1%), there is still a clear asymmetry. This asymmetry confirms the off-axis geometry of the grating, as such asymmetric population can not be achieved at normal incidence for traditional, axis-symmetric, gratings.

# REFERENCES

[1] T. K. Gaylord and M. Moharam, “Analysis and applications of optical diffraction by gratings,” *Proceedings of the IEEE* **73**, 894 (1985).

[2] D. C. Flanders, H. Kogelnik, R. V. Schmidt, and C. V. Shank, “Grating filters for thin-film optical waveguides,” *Appl. Phys. Lett.* **24**, 194 (1974).

[3] A. Basu and J. M. Ballantyne, “Second-and higher-order waveguide grating filters. 1: Theory,” *Appl. Optics* **18**, 3620 (1979).

[4] R. C. Enger and S. K. Case, “Optical elements with ultrahigh spatial-frequency surface corrugations,” *Appl. Optics* **22**, 3220 (1983).

[5] T. Tamir and S.-T. Peng, “Analysis and design of grating couplers,” *Appl. Phys.* **14**, 235 (1977).

[6] M. Li and S. J. Sheard, “Waveguide couplers using parallelogramic-shaped blazed gratings,” *Opt. Commun.* **109**, 239 (1994).

[7] Z. Guo and J. Xiao, “Ultracompact mode-order converting power splitter for mid-infrared wavelengths using an MMI coupler embedded with oblique subwavelength grating wires,” *Opt. Commun.* **488**, 126850 (2021).

[8] G. D. Boyd, L. A. Coldren, and F. G. Storz, “Directional reactive ion etching at oblique angles,” *Appl. Phys. Lett.* **36**, 583 (1980).

[9] J. Schrauwen, F. Van Laere, D. Van Thourhout, and R. Baets, “Focused-ion-beam fabrication of slanted grating couplers in silicon-on-insulator waveguides,” *IEEE Photonic Tech. L.* **19**, 816 (2007).

[10] J. M. Miller, N. de Beaucoudrey, P. Chavel, J. Turunen, and E. Cambril, “Design and fabrication of binary slanted surface-relief gratings for a planar optical interconnection,” *Appl. Optics* **36**, 5717 (1997).

[11] H. Wang, W. Zhang, D. Ladika, H. Yu, D. Gailevičius, H. Wang, *et al.*, "Two-Photon Polymerization Lithography for Optics and Photonics: Fundamentals, Materials, Technologies, and Applications," *Adv. Funct. Mater.* **33**, 2214211 (2023).

[12] S. Kawata, H. B. Sun, T. Tanaka, and K. Takada, "Finer features for functional microdevices," *Nature* **412**, 697 (2001).

[13] B. Wang, Q. Zhang, and M. Gu, "Aspherical microlenses enabled by two-photon direct laser writing for fiber-optical microendoscopy," *Opt. Mater. Express* **10**, 3174 (2020).

[14] F. Hou, Y. Zhan, S. Feng, J. Ye, X. Wang, W. Sun, and Y. Zhang, "Smart grating coupled whispering-gallery-mode microcavity on tip of multicore optical fiber with response enhancement," *Opt. Express* **30**, 25277 (2022).

[15] E. D. Lemma, F. Rizzi, T. Dattoma, B. Spagnolo, L. Sileo, A. Qualtieri, *et al.*, "Mechanical properties tunability of three-dimensional polymeric structures in two-photon lithography," *IEEE T. Nanotechnol.* **16**, 23 (2016).

[16] C. Accoto, A. Qualtieri, F. Pisanello, C. Ricciardi, C. F. Pirri, M. De Vittorio, and F. Rizzi, "Two-photon polymerization lithography and laser doppler vibrometry of a SU-8-based suspended microchannel resonator," *J. Microelectromech. Syst.* **24**, 1038 (2014).

[17] M. T. Raimondi, S. M. Eaton, M. M. Nava, M. Laganà, G. Cerullo, and R. Osellame, "Two-photon laser polymerization: from fundamentals to biomedical application in tissue engineering and regenerative medicine," *J. J. Appl. Biomater. Func.* **10**, 56 (2012).

[18] S. Kim, F. Qiu, S. Kim, A. Ghanbari, C. Moon, L. Zhang, *et al.*, "Fabrication

and characterization of magnetic microrobots for three-dimensional cell culture and targeted transportation," *Adv. Mater.* **25**, 5863 (2013).

[19] N. Rohbeck, R. Ramachandramoorthy, D. Casari, P. Schürch, T. E. Edwards, L. Schilinsky, *et al.*, "Effect of high strain rates and temperature on the micromechanical properties of 3D-printed polymer structures made by two-photon lithography," *Mater. Design* **195**, 108977 (2020).

[20] L. Pertoldi, V. Zega, C. Comi, and R. Osellame, "Dynamic mechanical characterization of two-photon-polymerized SZ2080 photoresist," *J. Appl. Phys.* **128**, 175102 (2020).

[21] J. Bauer, A. Guell Izard, Y. Zhang, T. Baldacchini, and L. Valdevit, "Programmable mechanical properties of two-photon polymerized materials: from nanowires to bulk," *Adv. Mater. Technol.* **4**, 1900146 (2019).

[22] I. S. Ladner, M. A. Cullinan, and S. K. Saha, "Tensile properties of polymer nanowires fabricated via two-photon lithography," *RSC Adv.* **9**, 28808 (2019).

[23] S. Chen, Y. Zhang, X. Hong, and J. Li, "Technologies and applications of silicon-based micro-optical electromechanical systems: A brief review," *J. Semicon.* **43**, 081301 (2022).

[24] H. Yu, P. Zhou, and W. Shen, "Fast-scan MOEMS mirror for HD laser projection applications," *2021 IEEE 16th International Conference on Nano/Micro Engineered and Molecular Systems (NEMS)*, 265 (2021).

[25] M. C. Wu, T. J. Seok, S. Han, and N. Quack, "Large-scale, MEMS-actauated silicon photonic switches," *2015 International Conference on Photonics in Switching (PS)*, 124 (2015).

[26] R. El Ahdab, S. Sharma, F. Nabki, and M. Ménard, "Wide-band silicon photonic MOEMS spectrometer requiring a single photodetector," *Opt. Express* **28**, 31345 (2020).

[27] V. P. Stinson, N. Shuchi, M. McLamb, G. D. Boreman, and T. Hofmann, "Mechanical Control of the Optical Bandgap in One-Dimensional Photonic Crystals," *Micromachines* **13**, 2248 (2022).

[28] V. P. Stinson, N. Shuchi, D. Louisos, M. Mclamb, G. D. Boreman, and T. Hofmann, "Photonic Crystals Fabricated by Two-Photon Polymerization with Mechanical Defects," *Optics* **4**, 300 (2023).

[29] C. Reinhardt, A. Ovsianikov, S. Passinger, and B. N. Chichkov, "Fabrication of micromechanical and microoptical systems by two-photon polymerization," *P. Soc. Photo.-Opt. Ins.* **6466**, 194 (2007).

[30] G. Williams, M. Hunt, B. Boehm, A. May, M. Taverne, D. Ho, *et al.*, "Two-photon lithography for 3D magnetic nanostructure fabrication," *Nano Res.* **11**, 845 (2018).

[31] M. Lata, Y. Li, S. Park, M. J. McLamb, and T. Hofmann, "Direct laser writing of birefringent photonic crystals for the infrared spectral range," *J. Vac. Sci. Technol. B* **37**, 062905 (2019).

[32] A. Hessel, J. Schmoys, and D. Tseng, "Bragg-angle blazing of diffraction gratings," *JOSA* **65**, 380 (1975).

[33] D. B. Fullager, G. D. Boreman, and T. Hofmann, "Infrared dielectric response of nanoscribe IP-dip and IP-L monomers after polymerization from 250 $\mathrm{cm}^{-1}$ to 6000 $\mathrm{cm}^{-1}$," *Opt. Mater. Express* **7**, 888 (2017).

[34] J. Durisova, D. Pudis, M. Goraus, and P. Gaso, "IP-Dip photoresist surfaces for photonic applications prepared by laser lithography and studied by AFM," *Appl. Surf. Sci.* **461**, 108 (2018).

[35] *Structural Mechanics Module User's Guide*, COMSOL Multiphysics, Burlington, MA, 198–243 (2023).

[36] K. R. Symon, *Mechanics*, Reading, MA, Addison-Wesley Publishing Company, (1971).

[37] X. Shang, N. Wang, Z. Wang, H. Jiang, Y. Jia, N. Zhou, and M. Qiu, "Customizable and highly sensitive 3d micro-springs produced by two-photon polymerizations with improved post-treatment processes," *Appl. Phys. Lett.* **120**, 171107 (2022).

[38] V. P. Stinson, U. Subash, M. K. Poutous, and T. Hofmann, "Towards Two-Photon Polymerization-Compatible Diffractive Optics for Micro-Mechanical Applications," *Micromachines* **14**, 1319 (2023).

[39] Y. Li, S. Park, M. McLamb, M. Lata, S. Schöche, D. Childers, I. Aggarwal, M. Poutous, G. Boreman, and T. Hofmann, "UV to NIR optical properties of IP-Dip, IP-L, and IP-S after two-photon polymerization determined by spectroscopic ellipsometry," *Opt. Mater. Express.* **9**, 4318 (2019).

[40] V. P. Stinson, S. Park, M. McLamb, G. Boreman, and T. Hofmann, "Photonic Crystals with a Defect Fabricated by Two-Photon Polymerization for the Infrared Spectral Range," *Optics* **2**, 284 (2021).

# CHAPTER 5: SUMMARY AND OUTLOOK

In this work, two-photon polymerization has been implemented to fabricate novel micro-structured optics. Both wavelength-scale and sub-wavelength scale structured optics were considered for these designs. Mechanically sensitive constituents were introduced to these designs in order to allow mechanical tuning.

In the first study, a static one-dimensional photonic crystal with an intentional defect was developed. A narrow transmission band was observed in the center of a photonic bandgap as a result of this defect layer. In order to exploit the photonic bandgaps' sensitivity to changes in layer thickness further, mechanical flexures were introduced to the low-density layers. By applying compression, it was observed that the photonic bandgap could be shifted to higher frequencies. It was also observed that the photonic bandgap shifted back towards lower frequencies as the compression was removed, verifying the elastic properties of the structure.

Combining the results of these two studies, a photonic crystal with a mechanical defect layer was designed. The thickness and fill factor of the defect layer was optimized such that upon compression a defect resonance would move into the photonic bandgap. The defect resonance shift was experimentally verified during compression and the resonance shifted outside of the bandgap as compression was removed, suggesting an elastic relaxation of the defect layer similar to the low-density design. In contrast to the low-density design, the photonic bandgap's amplitude and spectral center before and after compression was nearly identical. This is likely due to the rigid characteristics of low- and high-density layers in this design. These layers are the main contributors to the photonic bandgap's amplitude and center.

In order to allow more complex control of propagating light, wavelength-scale structured arrays were investigated. In this regime, diffractive optics can be developed. Like the photonic crystals, the optical response of diffractive gratings are very sensitive to geometric changes. A diffractive grating was designed such that the population of higher orders would be sensitive to changes in the geometry due to compression. Slanted wire gratings were selected for this investigation. Slanted wire gratings have an off-axis symmetry, by applying compression to the array, the slant angle of the grating can be varied. The grating was optimized to be sensitive to changes in slant angle. The design was mechanically characterized using finite-element method simulations. Following this numerical study, a slanted wire grating was fabricated by two-photon polymerization for visible operation for the first time. While the grating's diffractive characteristics deviated from the design, likely due to fabrication errors, the off-axis symmetry of the grating was confirmed.

One obstacle of fabricating structured optics by two-photon polymerization is scalability. For the designs presented in this work, the main applications will be in small scale settings such as integrated or fiber optics, or in the principle rapid prototyping of a design before large scale fabrication by an alternative approach. One advantage of this fabrication approach are that these three-dimensional structures can be printed directly on a device, such as a photonic integrated chip or fiber optic tip. As the need for compact dynamic processing power increases, the ability to fabricate nearly arbitrary structured optics with mechanical sensitivity may play a role in developing the next generation of technology.

# LIST OF OWN PUBLICATIONS

## PEER REVIEWED TECHNICAL ARTICLES

1. M. McLamb, Y. Li, **P. Stinson**, and T. Hofmann, “Metasurfaces for the Infrared Spectral Range Fabricated Using Two-Photon Polymerization,” *Thin Solid Films* **721**, 138548 (2021).

2. S. Park, **V. P. Stinson**, G. D. Boreman, and T. Hofmann, “Terahertz anisotropic response of additively manufactured one-dimensional photonic crystals,” *Opt. Lett.* **46**, 3396 (2021).

3. S. Park, **V. P. Stinson**, M. McLamb, G. D. Boreman, and T. Hofmann, “Mechanical tuning of defect modes in polymer-based terahertz one-dimensional photonic crystals fabricated by stereolithography,” *Opt. Eng.* **60**, 117104 (2021).

4. **V. P. Stinson**, S. Park, M. McLamb, G. Boreman, and T. Hofmann, “Photonic Crystals with a Defect Fabricated by Two-Photon Polymerization for the Infrared Spectral Range,” *Optics* **2**, 284 (2021).

5. M. McLamb, S. Park, **V. P. Stinson**, Y. Li, N. Shuchi, G. D. Boreman, and T. Hofmann, “Tuning of Reciprocal Plasmonic Metasurface Resonances by Ultra-Thin Conformal Coatings,” *Optics* **3**, 70 (2022).

6. **V. P. Stinson**, N. Shuchi, M. McLamb, G. D. Boreman, and T. Hofmann, “Mechanical Control of the Optical Bandgap in One-Dimensional Photonic Crystals,” *Micromachines* **13**, 2248 (2022).

7. **V. P. Stinson**, N. Shuchi, D. Louisos, M. McLamb, G. D. Boreman, and T. Hofmann, “Photonic Crystals Fabricated by Two-Photon Polymerization with Mechanical Defects,” *Optics* **4**, 300 (2023).

8. N. Shuchi, J. Mower, **V. P. Stinson**, M. J. McLamb, G. D. Boreman, M. G. Walter, and T. Hofmann, "Complex dielectric function of thiazolothiazole thin films determined by spectroscopic ellipsometry," *Opt. Mater. Express* **13**, 1589 (2023).

9. **V. P. Stinson**, U. Subash, M. K. Poutous, and T. Hofmann, "Towards Two-Photon Polymerization-Compatible Diffractive Optics for Micro-Mechanical Applications," *Micromachines* **14**, 1319 (2023).

## CONFERENCE PROCEEDINGS

1. **V. P. Stinson**, N. Shuchi, M. McLamb, G. D. Boreman, and T. Hofmann, "One-Dimensional Photonic Crystals with Narrow-Band Defect Modes Fabricated by Direct Laser Writing," *2022 IEEE Research and Applications of Defense Conference (RAPID)*, (2022).

2. M. McLamb, **V. P. Stinson**, N. Shuchi, G. D. Boreman, and T. Hofmann, "Frequency Tuning of Perfect Absorbing Metamaterial using a Thin Conformal Coating," *2022 IEEE Research and Applications of Defense Conference (RAPID)*, (2022).

3. M. McLamb, Y. Li, **V. P. Stinson**, N. Shuchi, D. Louisos, and T. Hofmann, "Bi-encoded metasurfaces for the infrared spectral range," *Optical Components and Materials XX* **12417**, SPIE, 101 (2023).

4. **V. P. Stinson**, N. Shuchi, M. McLamb, G. Boreman, and T. Hofmann, "Mechanical tunability in one-dimensional photonic crystals fabricated by direct laser writing," *MOEMS and Minitiarized Systems XXII* **12434**, SPIE, 24 (2023).

5. **V. P. Stinson**, U. Subash, M. K. Poutous, and T. Hofmann, “Mechanical Tuning of Diffractive Gratings Compatible with Two-Photon Polymerization,” *2023 IEEE Research and Applications of Defense Conference (RAPID)*, (2023).

6. M. McLamb, **V. P. Stinson**, N. Shuchi, G. D. Boreman, and T. Hofmann, “Frequency Selective Metasurface Fabricated with Two-Photon Polymerization,” *2023 IEEE Research and Applications of Defense Conference (RAPID)*, (2023).

7. **V. P. Stinson**, N. Shuchi, D. Louisos, M. McLamb, G. D. Boreman, and T. Hofmann, “One-dimensional photonic crystals with mechanical defects fabricated by two-photon polymerization,” *Optical Manipulation and Structured Materials Conference* **12606**, SPIE, 144 (2023).

8. M. McLamb, **V. P. Stinson**, N. Shuchi, D. Louisos, and T. Hofmann, “Switchable reciprocal metasurfaces for infrared scene projection,” *Optical Components and Materials XXI* **12882**, SPIE, 90 (2024).

9. N. Shuchi, T. Adams, **V. P. Stinson**, M. J. McLamb, D. Louisos, G. D. Boreman, M. Walter, and T. Hofmann, “Optical properties of photochromic thiazolothiazole-based polymer thin films determined by spectroscopic ellipsometry,” *Organic Photonic Materials and Devices XXVI* **12883**, SPIE, 55 (2024).

10. **V. P. Stinson**, U. Subash, N. Shuchi, M. K. Poutous, and T. Hofmann, “Dynamic polarization and mechanical tuning of slanted wire diffraction gratings,” *MOEMS and Minitiarized Systems XXIII* **12899**, SPIE, 1289902 (2024).

11. N. Shuchi, T. Adams, **V. P. Stinson**, M. McLamb, D. Louisos, G. D. Boreman, M. G. Walter, and T. Hofmann, "Complex Dielectric Function of Photochromic Thiazolothiazole Embedded Polymers Determined by Spectroscopic Ellipsometry," accepted for *CLEO: Science and Innovations*, Optica Publishing Group, (2024).

12. N. Shuchi, **V. P. Stinson**, U. Subash, M. K. Poutous, and T. Hofmann, "Mechanical Tuning of the Diffraction Efficiency of THz Slanted Wire Gratings," accepted for *CLEO: Science and Innovations*, Optica Publishing Group, (2024).

13. M. McLamb, **V. P. Stinson**, N. Shuchi, D. Louisos, and T. Hofmann, "Dynamic Reciprocal Plasmonic Metasurfaces for the Infrared Spectral Range," accepted for *CLEO: Fundamental Science*, Optica Publishing Group, (2024).

14. **V. P. Stinson**, U. Subash, N. Shuchi, M. K. Poutous, and T. Hofmann, "Slanted Wire Diffraction Gratings Fabricated by Two-Photon Polymerization," accepted for *CLEO: Science and Innovations*, Optica Publishing Group, (2024).